UC San Diego

UC San Diego Electronic Theses and Dissertations

Title

Vision and Wide-Field Imagers with Curved Focal Planes

Permalink

https://escholarship.org/uc/item/0x6144kf

Author

Arianpour, Ashkan

Publication Date

2015

Peer reviewed|Thesis/dissertation

eScholarship.org Powered by the California Digital Library
University of California

UNIVERSITY OF CALIFORNIA SAN DIEGO

Vision and Wide-Field Imagers with Curved Focal Planes

A dissertation submitted in partial satisfaction of the
requirements for the degree Doctor of Philosophy

in

Electrical Engineering (Photonics)

by

Ashkan Arianpour

Committee in charge:

Professor Joseph Ford, Chair
Professor Yuh-wa Lo, Co-Chair
Professor Michael Heller
Professor Truong Nguyen
Professor Kun Zhang

2015

Copyright

Ashkan Arianpour, 2015

All Rights Reserved.

The Dissertation of Ashkan Arianpour is approved, and it is acceptable in quality and form for publication on microfilm and electronically:

_____

_____

_____

_____

_____

Chair

University of California San Diego

2015

Dedication

To my family

Table of Contents

List of Figures

Acknowledgements

I would like to thank my advisors, Professor Joseph Ford and Professor Yuhwa Lo, for their guidance throughout my PhD. I've have the opportunity to work with some of the most intelligent people I've ever met while at UCSD. I would like to thank my committee members, Professor Truong Nugyen, Professor Michael Heller, and Professor Kun Zhang for their comments and guidance.

I would also like to thank the members of PSI Lab, Igor Stamenov, Nojan Motamedi, Salman Karbasi, Max Mellette, and Glenn Schuster. A special thanks to Professor Charles Tu as well for his guidance and trust.

The material in this dissertation is based on the following papers which are either published, or under final process for publication.

Chapter 2 is based on a reprint of the following paper: A. Arianpour, E. J. Tremblay, I. Stamenov, J. E. Ford, D. J. Schanzlin, and Y. Lo, "An Optomechanical Model Eye for Ophthalmological Refractive Studies," J. Refract. Surg. 29(2), 126-132.

Chapter 3 is based on a reprint of the following paper: A. Arianpour, G.M. Schuster, I. Stamenov, J. Ford, A. Groisman, J. Legerton, B. Meyers, G. Alonso, and E. Tremblay, "Wearable telescopic contact lens," Applied Optics (2015)

Chapter 4 is based on following paper: A. Arianpour, N. Motamedi, I. Agurok, and J. Ford, "Enhanced signal coupling in wide-field fiber-coupled imagers," Opt. Express 23, 5285-5299 (2015).

The dissertation author was the primary author of the work in these chapters, and the coauthor (Prof. Joseph Ford) has approved the use of the material for this dissertation.

Vita

2007	Bachelor of Science, University of California, San Diego, USA
2010	Master of Science in Electrical Engineering, University of California, San Diego, USA
2015	Doctor of Philosophy in Electrical Engineering, University of California, San Diego, USA

ABSTRACT OF THE DISSERTATION

Vision and Wide-Field Imagers with Curved Focal Planes

by

Ashkan Arianpour

Doctor of Philosophy in Electrical Engineering (Photonics)

University of California, San Diego, 2015

Professor Joseph Ford, Chair

Professor Yuhwa Lo, Co-Chair

This dissertation provides details regarding the implementation of curved-focal surface fiber coupled imaging for medical and wide-field applications. An optomechanical fluid-filled eye model with visual acuity better than 20/20 vision was design and characterized. A wearable telescopic contact lens was worn on the optomechanical eye model and the performance characterized. Measurements of the contact lens surfaces were modeled to quantify the impact of contact lens fabrication on end-result resolution. Separately, the limitations of the field of view in fiber coupled monocentric imaging are

analyzed. This dissertation describes a novel technique to address this based on conformal micro-optics. The design, simulation, and fabrication of an embossed surface relief micro-prism that increases the field of view are demonstrated.

1. Introduction

1.1 Curved Surface Imaging

The primary aberrations in an optical system, which are known as the Seidel aberrations, include: spherical, coma, astigmatism, distortion, and field curvature [1]. These aberrations impede an optical system by reducing the acquirable spatial resolution for the related F/# of the system. Wide angle imaging systems where ray trace approximations cannot be considered paraxial are extremely susceptible to geometrical aberrations as the field of view increases, or as the F/# decreases. Field curvature is an example of a geometrical aberration where rays from a flat object pass through a lens and come to a focus on a curved surface. The difficulty in designing a wide field of view imager lies in focusing all field angles onto a single flat plane while remaining diffraction-limited. In the current state of technology, digital cameras are limited to flat silicon-based detectors that are rigid and require multi-lens configurations to accommodate for the field curvature, in addition to other aberrations. Employing a curved focal surface instead of a flat focal plane can significantly reduce the number of optical components required, and increase the overall resolution of the system.

Curved focal surfaces can be found in nature as the image surfaces for visual systems. In the human eye, rays pass through the cornea to the crystalline lens where focus adjustment takes place, and end on the curved retina. Rods and cones residing on the retina

transmit the information to the brain where vision is interpreted and experienced, resulting in an extremely wide field of view system nearing between 200-220° with both eyes [2], a feature nearly unobtainable when compared to a conventional single-sensor wide field cameras. 20/20 vision is considered to be the nominal on-axis visual acuity of the eye, which translates to a resolution of approximately 30 cycles/° [3]. Inherent or age related defects can cause an individual's vision to deteriorate, requiring them to rely on visual aids or surgical operations for treatment. These visual aids must accommodate the mechanical, biological, and optical properties of the eye to be comfortably worn by patients, and must be designed for an imaging system with a curved focal surface.

A monocentric optical system is a configuration where all surfaces, including the focal surface, are concentric with respect the principal plane of the optic. This means that all field angles on the image surface are effectively on-axis [4] In wide-field imaging, monocentric lens systems are capable of achieving a low F/# and wide field view while remaining compact with a minimal number of optical components. In the first developments of this technology, the focal surfaces consisted of cylindrical films that were concentric about the center of the lens element [5]. However, a cylindrical geometry only eliminates the requirement to correct for field curvature in the longitudinal axis of the cylindrical geometry; the orthogonal axis of the focal surface remains flat. Under the current manufacturing methods, focal planes are broadly implemented as flat CMOS sensors, though the need for a curved focal sensor is pressing. In some of the recent developments for monocentric imaging, researchers constructed a multi-element monocentric lens with an array of relay imagers and flat focal sensors in a spherical geometry to create a stitched image of a wide field of view scene [6]. While the system

retains a high resolution, the size and expense of each of the components is impractical for commercial markets. An alternative is to use a curved input-face fiber bundle as a substitute for the focal surface, and bond the flat output-face of the fiber bundle to a flat CMOS imager.

1.2 Fiber coupled imaging

Fiber optics are composed of dielectric materials that act as waveguides confining and propagating light via total internal reflection from an input surface to an output surface. The waveguide is composed of a core and a surrounding cladding where the core index is greater than the cladding index. The index contrast between the core and cladding determines the angle of the acceptance of the waveguide, and is referred to as the numerical aperture (NA), where the angle of acceptance is related by $NA = \sin\theta_i$, and θ_i is the incident angle with respect to the normal of a planar input fiber. For imaging applications, high NA fibers are fused and bundled to create a quasi-periodic structure (Fig. 1).

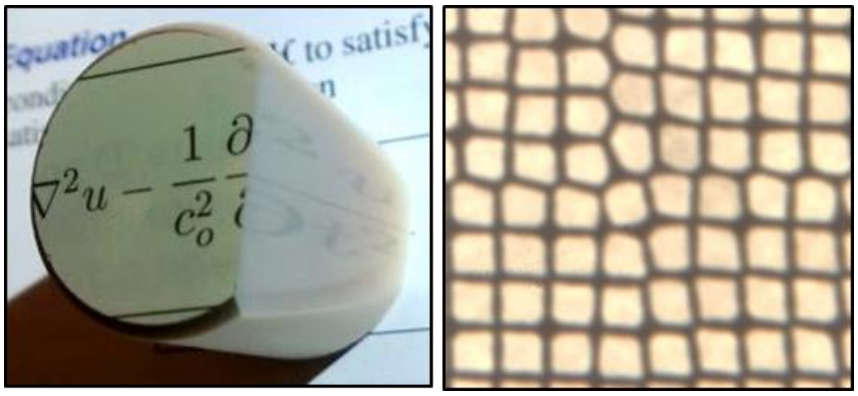

Figure 1-1: Left) Fiber bundle transmitting image from resting surface, (Right) Microscope image of a fiber bundle with a 4μm pitch.

Flat fiber bundles have been extensively integrated into endoscopic applications [7] Since fibers are able to transmit light from one input plane to another, using a curved-face fiber bundle as the focal surface can reduce both the number optical components and the geometrical aberrations associated with spherical lenses. A focusing beam incident on a curved-face bundle can propagate to a flat output where, as previously stated, an imaging sensor can be placed or the image relayed to create an effective curved imaging sensor.

Integrating curved-input fiber bundles into an optical system can benefit the overall resolution, but it also adds an additional step in the manufacturing process of digital image sensors. As previously mentioned, fiber bundles are quasi-periodic, and do not produce a seamless image.Furthermore, while the numerical aperture of the fibers can be 1, cross-talk from evanescent coupling is inevitable. Reducing the over size of the fibers and the inherent cross-talk can improve the fiber bundles performance in an imaging system.

1.3 Thesis organization

The dissertation is organized into the following sections: Chapter 2 illustrates the design and development of an optomechanical fluid-filled eye model with a curved focal plane as a retina. The optical design was modeled using a single-glass index for both the cornea and crystalline lens, optomechanics were constructed to create an adjustable focus system, and measurements of the visual acuity of the system are reported to be 20/20.

Chapter 3 details a wearable telescopic scleral lens with an imbedded unmagnified and magnified vision path. The contact lens was used in conjunction with the eye model to quantify the performance of the system, and demonstrate the duel unmagnified and

telescopic vision paths. Details regarding the metrology and fabrication process are included, and simulations illustrate the shortcomings of the optical performance.

Chapter 4 details a monocentric fiber coupled lens system with a curved focal surface and a beam deflector that enhances the field of view as a trade-off with signal-to-noise ratio and light collection. A design, simulation, and fabrication of the system is reported with characterizations of the overall system performance.

Chapter 5 consists of a brief conclusion of the overall work, detailing the advantages of curved focal surfaces and potential future directions for technology transitioning.

2. Optomechanical fluid-filled eye model

2.1 Overview

Vision-based devices (i.e. contact lenses, head mounted displays, intraocular lenses) are increasingly becoming more common among developers and consumers. The development of these new technologies can significantly benefit from a physical testing apparatus in the form of an optical life-sized eye model. As an example, the development cycle of IOLs are lengthy, and the process costly, especially attributable to the requisite testing on primates, which have accommodation mechanisms comparable to humans [8]. Moreover, assessment of the quality of vision over the range of accommodation is lacking in animal studies. Finally, a significant number of claims made by patients after surgery about poor visual acuity are related to incorrect measurements of patient biometry and the selection of IOLs [9]. A life-sized eye model capable of evaluating vision restoration after crystalline lens replacement with an IOL would be of great value in both ophthalmology research and in eye clinics, and would be a much welcomed addition to current biometric technologies [10,11]. Such a device would allow ophthalmologists to analyze optical images unprocessed by the brain. The device could aid the design and research of the intraocular lens or contact lens since characterizing a single lens component by experiment or simulation cannot produce the same amount of relevant information as characterizing the lens within a complete, real-size eye model. The device becomes even more attractive

when its dimensions and geometry can be adjusted easily to best match the eye structure of a patient. This would allow doctors to be able to select the most fitting intraocular lens for the patient and obtain quantitative information about the anticipated vision recovery before surgery. As a result, such a device holds promise to significantly improve the success rate and outcomes of cataract surgery, which is performed nearly 2 million times a year.

Prior to our work, other efforts exist to fabricate eye models to recreate images using crystalline lenses or IOLs [12,13,14,15,16,17,18] for assessment of the quality of soft contact lenses [19]. Most of these eye models use glass or polymer lenses to either directly couple the images to a CMOS sensor or transfer the images to the CMOS sensor via an optical relay system. Since the human retina forms a curved image surface that naturally corrects the effect of field curvature, but all existing eye models do not contain such capabilities, none of the these eye models accurately depicts the field of view and the true image quality. This deficiency seriously hinders the usage of existing eye models in clinics or IOL development. The most salient feature of our eye model, aside from its realistic dimensions, is the custom optics at the retina position to map the curved image surface to a flat image plane compatible with the CMOS imager. The optics introduces no optical artifacts and can faithfully transform the image formed on the retina surface onto an image sensor. By developing a glass lens model we are able to test the system under known conditions and compare our results when implementing additional optics. In short, we present in this paper a life-size, cost-effective, and fluid-filled optomechanical eye model that can reliably reproduce the structures and functions of all image-forming components

in human eye, including the cornea, aqueous humor, crystalline lens, vitreous humor, and retina.

2.2 Lens design

We chose a fused-silica lens based system to make the equivalent of the crystalline lens and cornea in the human eye and with matching optical power. The crystalline lens in the human eye has a graded refractive index ranging from 1.38 to 1.4 [20]. Reproducing such a graded index profile is technically challenging and would not provide significant improvements to the image resolution. Consequently, the silica lenses in our optomechanical eye model have a uniform index of refraction optimized for image quality along the optical axis. A set of optic components was then configured to match the on-axis characteristics of a specific human eye. Simulations and measurements were performed to assure the difference in the small-angle off-axis image quality between the specific human eye and the modeled eye is minimal within the macular area. The optomechanical eye model was designed and constructed in ways that all the components can be easily replaced and the housing has the flexibility of accommodating varying dimensions, such as distances between any optical surfaces.

The design of optomechanical eye model starts with ray-tracing simulations using the ZEMAX software. We used the widely-accepted Navarro model to represent the human eye and found the optimal parameters for our optomechanical eye model to closely match the image quality between our device and the Navarro human eye model [21].

Our model uses fused silica optics with a refractive index of 1.45. We use a cornea lens of 1mm thickness with an anterior radius of 7.8mm (conic constant: -0.5) [22] and a

posterior radius of 6.7mm. Our larger thickness was chosen to improve the durability of the lens; and simulations indicated this has a negligible effect on the resolution of the image. The fused silica lens that functions as the crystalline lens has an aspheric shape to minimize spherical aberration.

Most uniquely, at the position of the retina we constructed a closely-packed curved fiber bundle matching the profile of the retina as the image surface. The curved fiber bundle consists of an array of optical fibers with a core diameter of 4μm and a center-to-center spacing of 4.2μm. The bundled fiber has an anterior radius of curvature of 11.019mm to simulate the curvature of the retina and a flat posterior surface to allow image transformation onto a CMOS imager (6.4um pixel size) using relay at optics with a magnification of 2x. The specially designed fiber bundle was fabricated by Schott North America. The integrated curved fiber bundle provides a field-of-view of 34.5 degrees, which is significantly larger than the field-of-view of the fovea in human eye, thus allowing us to evaluate the image quality both in the macular area and in the peripheral vision. The 4.2μm core-to-core spacing yields a spatial resolution of approximately 120 cycles/mm that is comparable to the resolution of the macular area of the retina.

We treat each 4μm diameter fiber as one pixel that carries light of all colors to the RGB pixels on the CMOS image. This closely resembles how light propagates within the eye and reaches the photoreceptors in the cones and rods on the retina. Figure 1 shows the microscopic view of the bundled fiber. The white spots are the core of the fibers and the black areas are insulating rods that prevent crosstalk between the fibers. The image can be transmitted through the curved surface to the flat side of the fiber bundle and either detected directly or optically relayed to a CMOS imager. In practice, since the photosensitive area

of a CMOS imager is beneath a protective glass cover, the light from the fiber bundle cannot be perfectly coupled to the image sensor. Consequently, we prefer to use an optical relay to transmit the image from the flat side to an imaging sensor. The material composition of the curved fiber bundle is proprietary; however, the refractive indices of the core and cladding are 1.82 and 1.485, respectively, producing a numerical aperture (NA) of 1 [23].

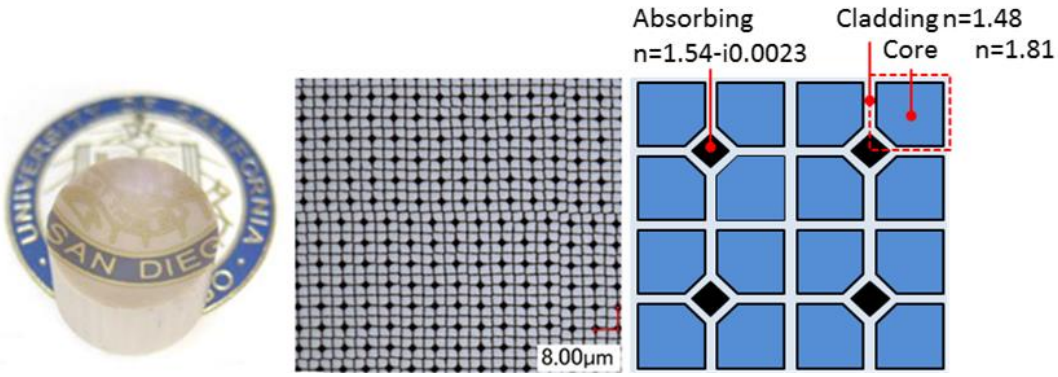

Figure 2-1: a) Curved fiber bundle transmitting image from UCSD logo. b) Microscopic view of fiber bundle. The white spots are the core of the fibers and the black areas insulating rods.

2.3 Optomechanical design

For the mechanical design of our eye model, we machined the optomechanical housing of a 28mm diameter delrin sphere for the mechanical design of the optomechanical eye model. All of the optical components were mounted to the housing so the spacing between any two elements may be adjusted to match the anatomy of individual patients' eyes. We created an insert for the cornea and used ultraviolet curable epoxy to mount it to the housing as the first optical element to prevent water leakage. We threaded a 10mm hole for inserting the pupil and the lens that simulates either the crystalline lens or the IOL. The lens is situated between a ring of 1mm thickness and a 3.75mm diameter pupil. The pupil

size can be varied by simply substituting a ring with a different inner diameter. By measuring the microscope focal distance to the surface of each element during assembly, we ensured all elements were aligned and correctly spaced to match the eye of interest. The errors in position of the optical elements depend on the accuracy of the microscope used for assembly and the operation errors in adjusting the microscope focus--the latter is on the order of tens of microns. We then used a clamp to hold the curved fiber bundle as shown in Figure 2(b). The clamp has 3 holes for springs and screws (M2x0.4) to allow adjustments of the tilt and position. Each 90 degree rotation of a screw accounts for the fiber bundle to move along the direction of the channel. An o-ring in the back of the optomechanical eye model holds the curved fiber bundle in place and prevents water leakage (Figure 2). The threaded area also acts as baffles that limit the scatter of light off the walls. Channels were created on the top and bottom surfaces to act as inlet and outlet during water filling. We vacuum filled the assembled optomechanical eye model using distilled water with a refractive index of 1.334 [12,24] to remove trapped gas bubbles. Water was used as the medium because the index of water is very close (within 1%) to the index of aqueous humor and vitreous humor.

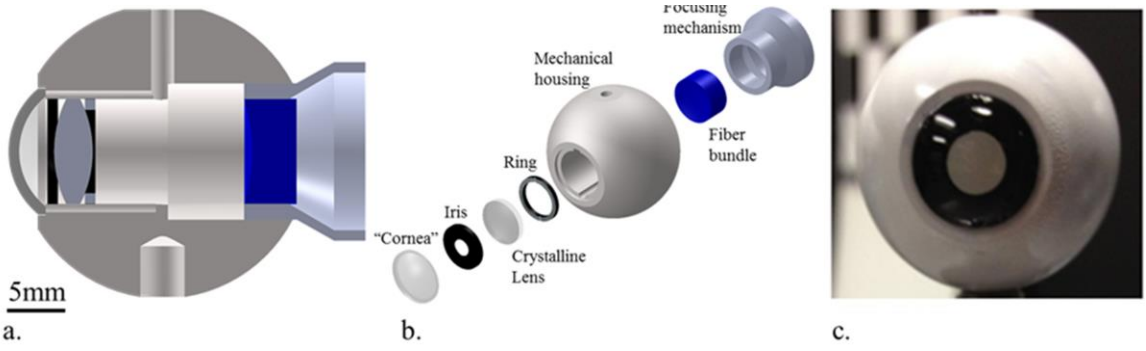

Figure 2-2: a) Cross-sectional view of optomechanical eye model; b) Exploded view with individual parts listed; c) The assembled optomechanical eye model that is comparable to a life-size human eye.

2.4 Ray-tracing simulation

ZEMAX was utilized to simulate the resolution and quantify the aberrations of each optical component for the optomechanical eye model and the Navarro model (Figures 3 and 4). All simulations were performed under polychromatic illumination with objects from an infinite distance and a pupil of 3.75mm diameter. Figure 3 shows that both the 0-degree and 5-degree off-axis images of our optomechanical eye model have similar resolution to that of the Navarro model. Both the Navarro model and the optomechanical eye model diminish in resolution with increasing field of view, but the resolution of the optomechanical eye model diminishes more quickly. Detailed analysis on optical aberrations as shown in Figure 4 demonstrates the Navarro model has lower coma than our optomechanical eye model. On the other hand, our optomechanical eye model has less spherical aberration and astigmatism than the Navarro model. The distortion and field curvature are nearly identical in both models.

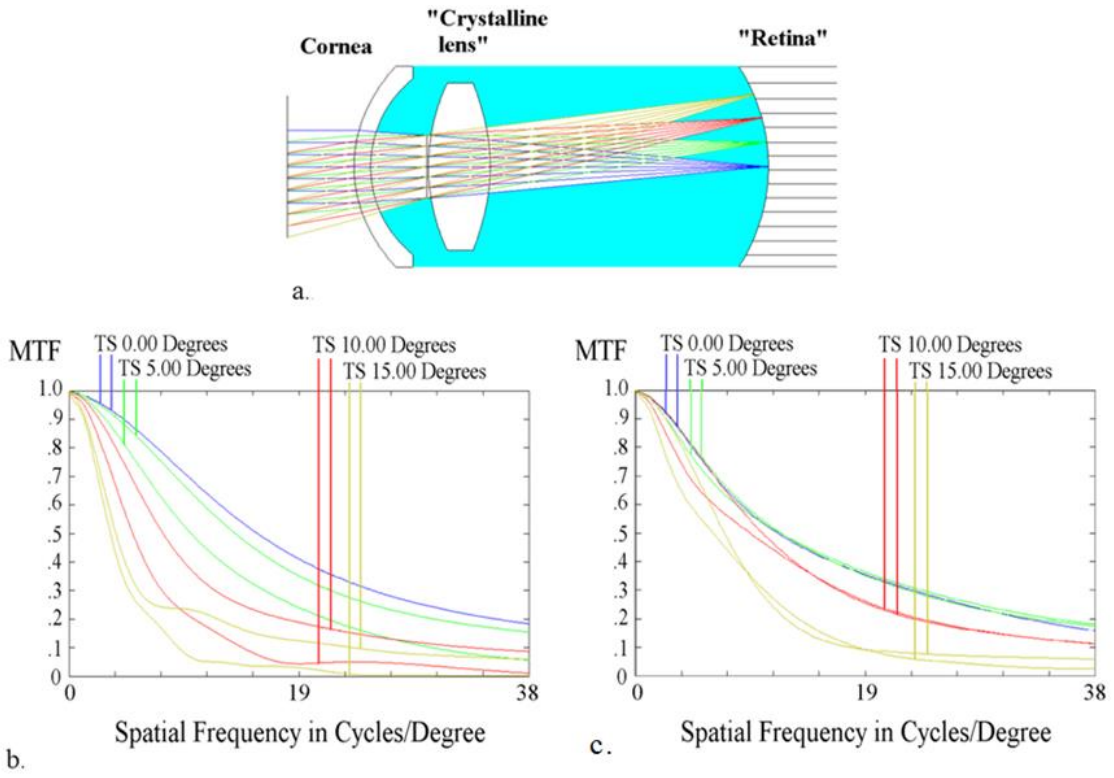

Figure 2-3: a) Optical simulation of the optomechanical eye model using ZEMAX software; (b,c): Polychromatic modulation transfer function (MTF) of our experimental optomechanical eye model and Navarro eye, respectively, with a 4mm pupil at an infinite conjugate.

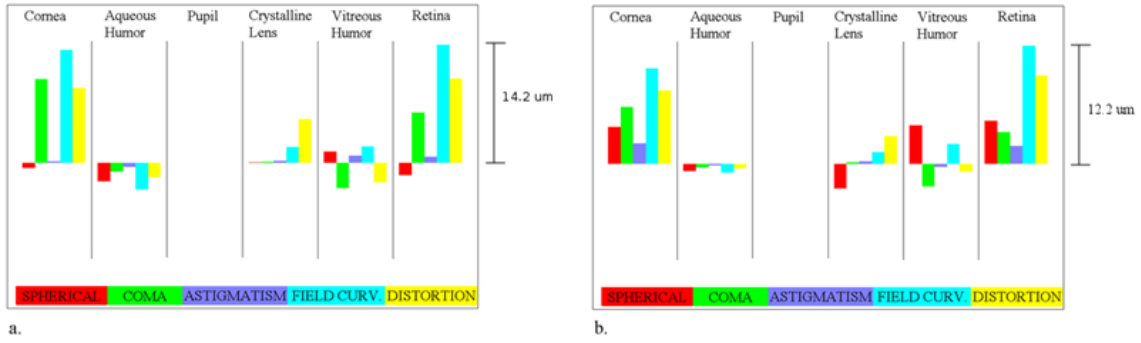

Figure 2-4: a,b) Calculated Seidel aberration coefficients of each individual surface and their summation on the retina for the optomechanical eye model and the Navarro model, respectively. Both diagrams are calculated at a wavelength of 550nm.

2.5 Characterizing optomechanical eye model

To characterize the optical properties of the optomechanical eye model we measured the image sharpness of a slanted edge on a black and white chart, a standard technique for measuring the resolution of digital cameras. Utilizing the optical assessment software, SFR Plus (Imatest) [25], we compared the modulation transfer function (MTF) produced by our optomechanical eye model at an infinite conjugate with the ZEMAX simulated MTF. The results enable us to assess the quality of device fabrication and assembly. Imatest measures sharpness by first obtaining the line spread function (LSF) of image of a slanted edge and then converting the LSF into spatial frequency, as a measure of the resolution of the device. This resolution is calculated in cycles or line-pairs per degree (cycles/degree or lp/degree). We adjusted the focal distance of the optomechanical eye model by moving the curved fiber bundle along the optical axis. To eliminate the constraints imposed by the mechanical assembly of commercial CMOS imagers, we used an optical relay system and a Canon EOS 5D Mark II camera (f-number: F/2.8, focal length of 100mm, and exposure time: 0.3 seconds) to capture the image projected on the surface of the curved fiber bundle. Since the relay optics transforms the image from the flat, rear surface of the fiber bundle to another flat CMOS imager plane, this step introduces negligible artifacts to the image. Limited by the size (4μm) of the individual fiber in the fiber bundle, the maximum achievable MTF is 38 cycles/degree. At 10% modulation depth, we obtained an on-axis resolution of approximately 34.0 cycles/degree and 33.1 cycles/degree for the horizontal and vertical MTF's, respectively. At 10 degrees off axis, the resolution becomes 7.8 cycles/degree and 8.8 cycles/degree for horizontal and vertical MTF's, respectively (Figure 5). Although resolution targets provide quantitative

assessments of the model's resolution, images of normal objects obtained in daily life under daylight conditions provide more relevant information of the characteristics of eye. Figure 6 shows an image of the Stone Bear on UCSD campus from a distance of approximately 25 meters, obtained by the optomechanical eye model. The curved surface of the fiber bundle matches the curvature of the retina, but all the fibers are packed in parallel with each other along the optical axis. When an image is formed on the curved surface and transmitted along the fiber, the image appears to be darker near the outer area.

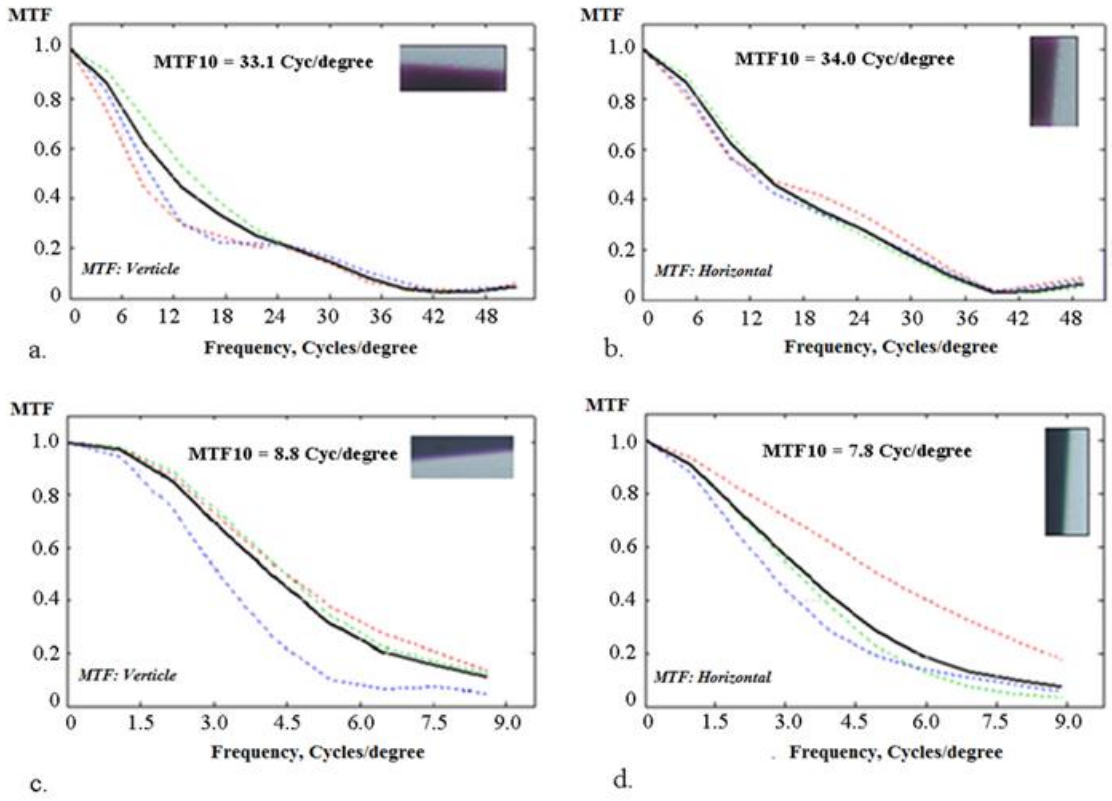

Figure 2-5: a,b) On-axis polychromatic MTF measured from the optomechanical eye model using a slanted edge chart; c,d) 10 degrees off-axis MTF measured from the eye model using the slanted edge chart. Images are illumined using fluorescent lighting. The images of the slanted edge chart are shown in the insets.

Figure 2-6: Image of the Stone Bear on UCSD campus. The object is approximately 25 meters from the optomechanical eye model. The darkening around the edges is caused by the limitation of the numerical aperture of the fiber and its inability to couple light efficiently at high fields of view, similar to the Stiles-Crawford effect. The red circular area represents the equivalent of the macular region in human eye.

We used the optomechanical eye model to evaluate IOLs by characterizing two commercial AcrySoft™ IOLs: one diffractive IOL and one refractive IOL. Both IOLs have the same optical power of 16 diopters with an iris of approximately 3mm. The IOLs were

centered on a ring with the edges glued to the fixture. Their haptics were removed to fit the housing. Situated at the position of the crystalline lens in the optomechanical eye model with the front surface of the IOL approximately 4.0mm from the back surface of the cornea, preliminary results of the lenses were characterized using a modified USAF 1951 resolution chart that was back lit by a halogen lamp for a qualitative comparison of the properties of two different IOLs. Figures 7(a) and (d) show images from both IOLs at an object distance of 15 feet. Then we took images at three feet (Fig. 7 (b, c)) and one foot (Fig. 7 (e, f)) from the resolution chart. In Figures 7(a) and (d), we converted the images to grayscale, cropped, and digitally zoomed to the center portion of the images. The spatial frequency bars that can be resolved are highlight and listed in the figures.

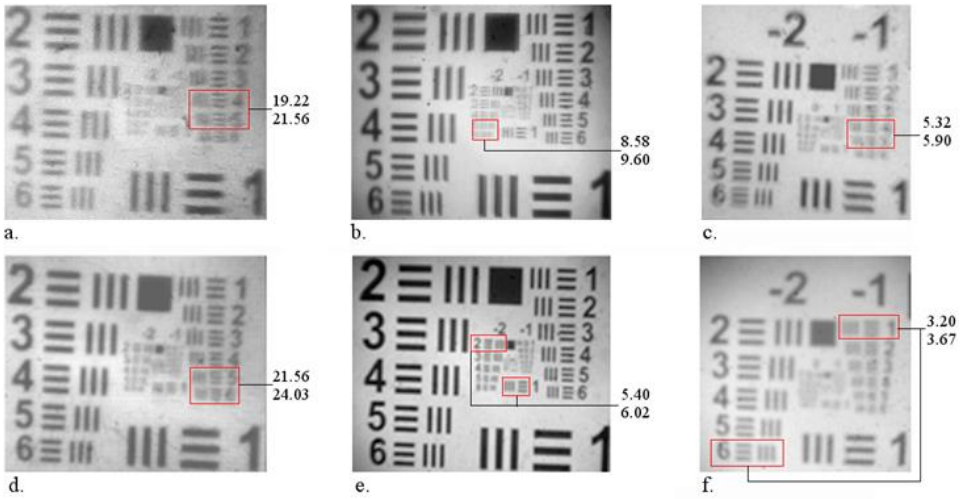

Figure 2-7: a-c) Images of the USAF 1951 resolution chart taken by the optomechanical eye model with a diffractive IOL at distances of 15 feet, 3 feet, and 1 foot. d-f) Same images taken by the optomechanical eye model with a refractive IOL at distances of 15 feet, 3 feet, and 1 foot. Grayscale conversion, digital zoom and cropping have been used to show the same features from images of different magnifications.

2.6 Analysis of optomechanical eye model

Close examination of the Imatest results show that the on-axis values of the optomechanical eye model match the resolution of healthy human eye with a horizontal and vertical combined average of 33.5 cycles/degree, better than 20/20 vision. The resolution is still lower than the ZEMAX-simulated value--this may be attributed to the manufacturing tolerances and positions of our lenses and a possible tilt in our mounting of the curved fiber bundle. Figure 8 shows the Monte Carlo simulation using ZEMAX to reveal performance degradation due to manufacturing tolerances (thickness, radius, and astigmatism) and component misalignments within 0.1mm and 1 degree tilt (2 degrees for the curved fiber bundle). As shown in Figure 8, our experimental data for the on-axis resolution is significantly better than the calculated scenario, indicating the manufacturing and assembly errors are lower than the magnitudes used in the simulation. While the cornea of our model does overcompensate for the spherical aberration in comparison to the Navarro model, the overall resolution of our eye model is significantly better than 20/20 vision. Additionally, we can further reduce the tolerances on the tilt and decentration of the curved fiber bundle by using a clamp with a single screw mechanism that would allow the fiber bundle to move easily along the optical axis.

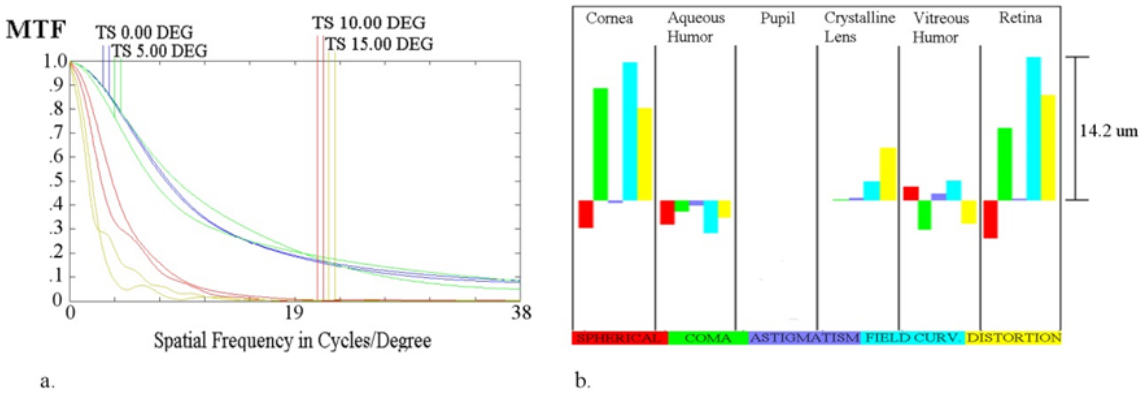

Figure 2-8: Potential scenario of loss of resolution due to manufacturing and assembly tolerances. (b) Potential scenario of calculated Seidel aberration coefficients from manufacturing and assembly tolerances.

Our optomechanical eye model also experiences a darkening along the edges at the posterior side of the bundle. This is due to the incident angles on the curved fiber bundle refracting and emitting at larger angles with respect to the optical axis as the field of view increases (Figure 9). Since our optical relay has a limited numerical aperture, it is unable to capture all of the light emitted from all of the fibers. The emission from the fiber bundle is not uniformly distributed across each of the solid angles, allowing for more light to be captured by the optical relay than calculated. Using a tapered fiber bundle with all the fibers oriented to be normal to the incident angles from any field of view will reducing the darkening affect along the edges. The light would be guided within the fiber with limited differences to the emitted solid angles from all of the fibers, producing a more uniform intensity profile.

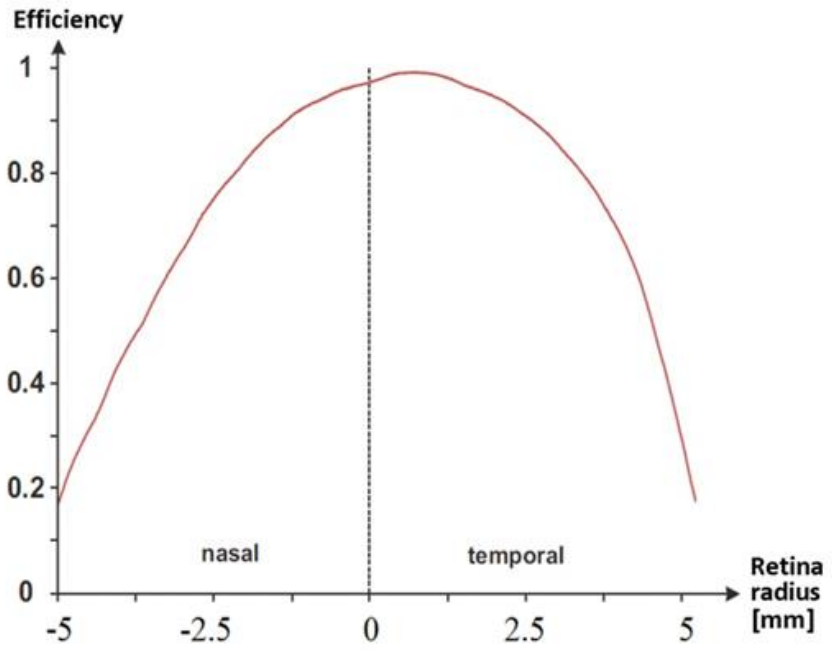

Figure 2-9: Relative intensity distribution across the fiber bundle along its vertical axis. The screen was uniformly illuminated at an angle with respect to our optomechanical eye model causing the tilt in the relative intensity plot.

Preliminary results with IOLs indicate that the multifocal IOL had a better depth of focus in comparison to the refractive IOL, as expected from the multifocal nature of the diffractive IOL. In our current optomechanical eye model, the achievable resolution of the IOL is generally lower than that of glass lenses due to difficulties in aligning the IOLs. The magnitudes of decentering and tilting errors are larger for IOLs since the area allotted for the IOL assembly is significantly greater than 0.1mm, yielding a larger alignment error during assembly. This problem can be remedied in future optomechanical eye models by incorporating the haptics into the optomechanical design and creating a more accurate mounting fixture.

2.7 Conclusion

To conclude, we demonstrated a life-size optomechanical eye model that can produce a resolution similar to the raw images projected onto human retina. The optomechanical design of the eye model can be easily customized to model the eyes of individual patients, thus offering ophthalmologists the capability to visualize the unprocessed images produced by different combinations of lenses and visual effects. The design offers easy ways to adjust the position of the curved fiber bundle and lens replacement, as well as the distance between any two optical surfaces in the eye model. The optomechanical eye model is fluid filled to simulate the aqueous humor and vitreous humor of human eye, and can simulate cataracts, myopia, hyperopia, and other defects. The use of the curved fiber bundle closely emulates the retina, and the flat posterior surface of the fiber bundle allows for transformation of the image to a CMOS camera. The optomechanical eye model is accurate, versatile, and cost-effective. Future improvements will further increase the potential to serve as a useful tool for clinical ophthalmology and development of medical optics such as contact lens and IOLs. The optomechanical model eye can also find applications in other optical instruments for vision inspection and research.

Chapter 2 is based entirely on the following paper: Arianpour A, Tremblay E.J, Stamenov I, Ford JE, Schanzlin DJ, Lo Y. “An Optomechanical Model Eye for Ophthalmological Refractive Studies,” J Refract Surg. 2013 Feb; 29(2):126-32

3. Wearable telescopic contact lens

3.1 Introduction

Age related macular degeneration (AMD) is an aging related ailment and the leading cause of blindness for individuals over the age of 55 [26], affecting an estimated 30-50 million worldwide. Some AMD patients rely on low magnification telescopic visual aids, magnifying the object scene and increasing the effective image resolution in the region outside of the fovea [27]. These telescopes are typically field glasses attached to eyewear [28], requiring continuous head motion for viewing of extended scenes [29].]. Recently, miniaturized telescopes have been surgically implanted into the crystalline lens of one eye, the other eye remaining unmodified [30]. These telescopes provide a 2.2x or 2.7x magnification and a 20˚ field of view that moves with the direction of gaze. This eye-borne magnification allows for more natural eye movement and interpersonal interactions. However, the available volume inside the crystalline lens restricts the aperture to a relatively large F/# of 12.5, limiting effective use to well-lit environments.

A low vision telescope in the form of a contact lens is a less invasive and more attractive solution. In 1963 an eye-borne 2x telescope was demonstrated as a visual aid for macular degeneration patients [31]. Two lenses and an aperture stop formed a refractive Galilean telescope, which was encapsulated within a 4.4mm thick scleral contact lens. However, this lens is too thick to be worn comfortably, and simply scaling the refractive

telescope to a sufficiently short length to fit comfortably would reduce the telescope aperture and resolution below a usable level.

A potential solution is to employ the geometry of a thin multiple-reflection telescope with an outer annular aperture [32]. This geometry has the advantage of reducing overall lens thickness by a factor equal to approximately the number of internal reflections, and also offers a central clear lens aperture which can be used to provide a separate optical path for unmagnified normal vision. We earlier described [33] a 1.1 mm thick switchable telescopic lens that provided both 1x and 2.8x magnification (Fig. 1) vision paths. This lens was successfully fabricated and tested on a scale model of the human eye (Fig. 2). Adding an external linear polarizer to the 1x path, we demonstrated a basic level of switching by selectively blocking the 1x path with an orthogonal polarization and liquid crystal shutter. However, this first "Generation-0" lens was a proof-of-principal optic unsuitable for human use. The internal reflection telescope had sharp external edges which would need to be encapsulated within a smooth casing to be made wearable, which forces significant optical redesign. In addition, the cornea requires a continuous flow of environmental oxygen, as it lacks the blood vessels which oxygenate normal tissue. The 1.1 mm thick GEN-0 lens PMMA (Polymethyl methacrylate) structure is impermeably to oxygen, allowing only short term (less than one hour) wear before it would begin causing pain, and potentially damage, to the cornea.

This paper describes the design, fabrication, and test of a version of this lens suitable for comfortable human wear, at least for the short term, and to show methods that can allow a version compatible with extended wear. To do this, we require the telescope be integrated as an optical "payload" embedded within the structure of a scleral lens, and

be modifiable to accommodate the user's vision correction prescription. We also changed the design to allow for switching between telescopic vision and a 1x vision mode that allows wide field peripheral vision. The chapter is organized as follows. Section 2 describes the proposed mechanical and optical design for the lens to be wearable on a human eye. Section 3 details the fabrication process and metrology regarding both the folded optic and scleral lens. Section 4 details the methods for testing the assembled scleral lens on an optomechanical eye model and the measured resolution for both unmagnified and telescopic vision. Section 5 describes the limitations of the fabricated optic, and Section 6 provides a demonstration of a proof of concept telescopic scleral lens in an exploratory clinical trial.

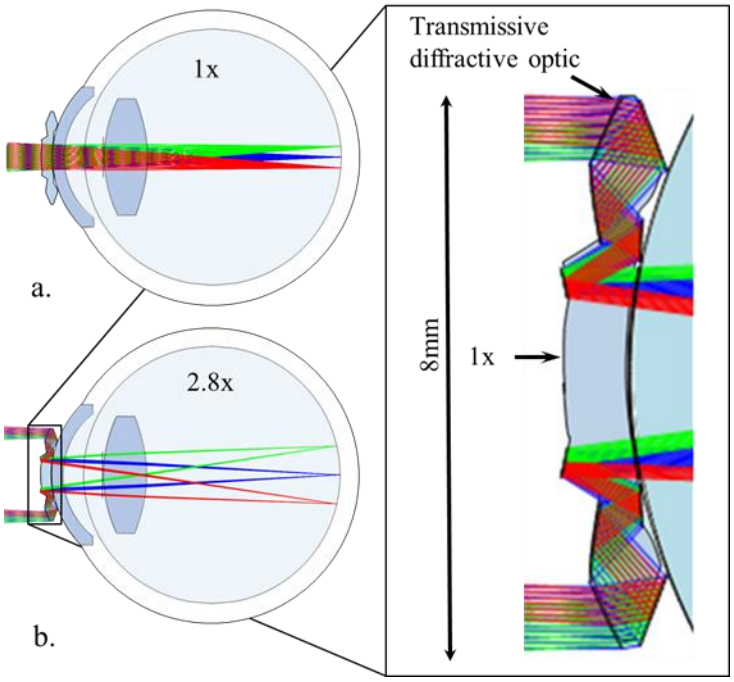

Figure 3-1: Generation-0 (not wearable) reflective telescopic contact lens with (a) 1x and (b) 2.8x vision paths.

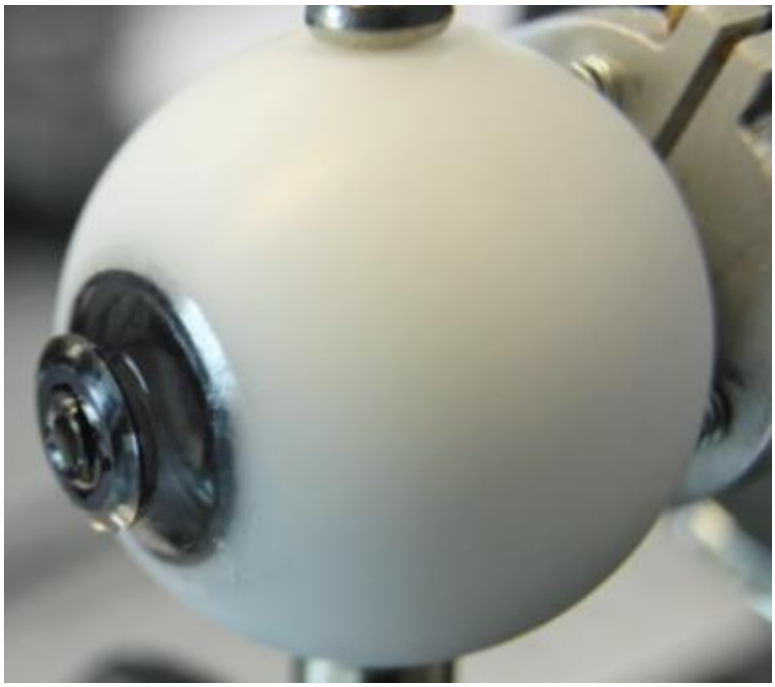

Figure 3-2: Generation-0 (not wearable) telescopic contact lens on an optomechanical eye model used for testing.

3.2 Wearable lens design

There are three major categories of contact lenses, the familiar soft contact lenses, and the less common rigid lenses in both corneal and scleral lens form. Soft lenses are made of a flexible gas-permeable polymer, inexpensively mass produced by molding. The lenses are typically up to 14.5mm in diameter and 84-230μm thick [34]. Though comfortable to wear, these materials are too flexible to hold the telescope mirror surfaces with sufficient precision. Rigid corneal diameter lenses (typically 8-10 mm diameter) can support the telescopic surfaces but are too thin. Corneal lens thickness is constrained by user comfort, because each time the user blinks, the eyelid must glide over the edge of the lens. They are also not accurately centered. Because the cornea surface is nearly spherical, corneal lenses allow significant lateral movement over the pupil. Scleral lenses are larger,

typically from 12.9-24mm in diameter [35], mounting on the white scleral region of the eye. Scleral lenses are commercially manufactured for special vision needs, including patients with highly irregular corneas. Each lens is diamond turned to the user's physical eye geometry and vision prescription by companies such as Paragon Vision Sciences. Scleral lenses can be comfortable with center thicknesses up to 2mm in thickness [36] because the user's eyelid remains on the scleral lens, and does not need to glide over the edge of the lens when blinking. Second, because the sclera is not perfectly spherical, a properly designed scleral lens is more stable than a corneal lens in both lateral and rotational motion [37].

Light collection of the concentric folded telescope is given by the area of the annular input aperture, which depends on the aspect ratio of the optic's thickness and the overall diameter, which is a function of the number of reflections used. A discussion of the scaling properties of concentric reflective imaging lenses can be found in reference [32]. and the characteristics of an afocal telescope geometry are similar. Light collection increases with lens diameter, which given the constraints on aspect ratio means that the lens center thickness also increases. Setting as a requirement a magnification close to 3x, we found that 2-reflection designs did not provide sufficient magnification, and that 6- and higher reflection designs introduced too much aperture obscuration (and extremely tight tolerances). A 4-reflection lens with a center thickness of 1 mm (as in the Gen 0 lens) is necessary for sufficient resolution and light collection. The result is that a relatively thick scleral lens provides the most favorable geometry for the contact lens telescope optics.

3.2.1 **Design for oxygenation**

Providing continuous oxygenation to the cornea is essential for both corneal and scleral contact lenses to be suitable for full-day wear. The Gen 0 lens was made of a standard PMMA optical plastic, which is straightforward to diamond turn and mirror coat. PMMA is biocompatible, but it is also essentially impermeable to oxygen. One of the original goals of this research project was to investigate the use of rigid gas permeable polymers for all of the internal lens structures. Optical designs using various gas permeable polymer materials were successful, but the mirror coatings introduced two practical limitations. First, high reflectivity mirror coatings themselves acted as oxygen barriers. The mirror can be made permeable using sub-wavelength patterning (i.e., a lossy fine-structure halftone pattern or nano-stuctured plasmonic mirrors). But a second practical limitation was that the deposition of high quality mirrors onto gas permeable materials proved difficult. Mirrors of good quality were deposited but were not physically robust, and did not survive integration into the outer housing. More fundamentally, oxygen flow through 1 mm of even the most gas permeable materials available was insufficient for reliable corneal oxygenation. Currently available rigid gas permeable lenses provide sufficient oxygenation with Dk values ranging from 100-165 [38]. The most permeable RGP material available, Silicon Elastomer, has a Dk of 340, enabling thicknesses up to 0.71mm [39]. But lens performance with this thickness constraint was unfavorable. Given these challenges, we looked for solutions to oxygenation that would enable the central "payload" to be entirely gas impermeable. One possibility was to provide an oxygenated fluid under a substantially gas impermeable lens. Perfluorocarbon liquids (PFCL) are one biocompatible candidate [40]. The 185µl volume under a scleral lens may support a day-

long reservoir of special PFCL contact lens solution. In addition, we investigated oxygenation via a structural as opposed to materials-based approach. Gas diffuses within a continuous open volume, even one with relatively small passages, significantly more easily than through even a thin layer of gas permeable plastic. So we considered a contact lens that holds a gas impermeable optical "payload" over a contiguous internal volume that extends over the cornea. Figure 3a shows the basic structure. Oxygen enters the water-tight volume through a relatively thin outer cover that includes a significant surface area on the lens periphery. Oxygen consumed by corneal tissue is replaced by flow under the gas impermeable payload, through a similarly thin inner cover over the central (corneal) region. The overall structure is supported by internal supports between the inner and outer shells, as shown in Fig. 3b. Since the surface area exposed to the outer air can be larger than the 10mm diameter oxygen-consuming cornea, as long as diffusion under the gas impermeable payload, the overall oxygen flow is substantially mediated by the thin layer over the cornea.

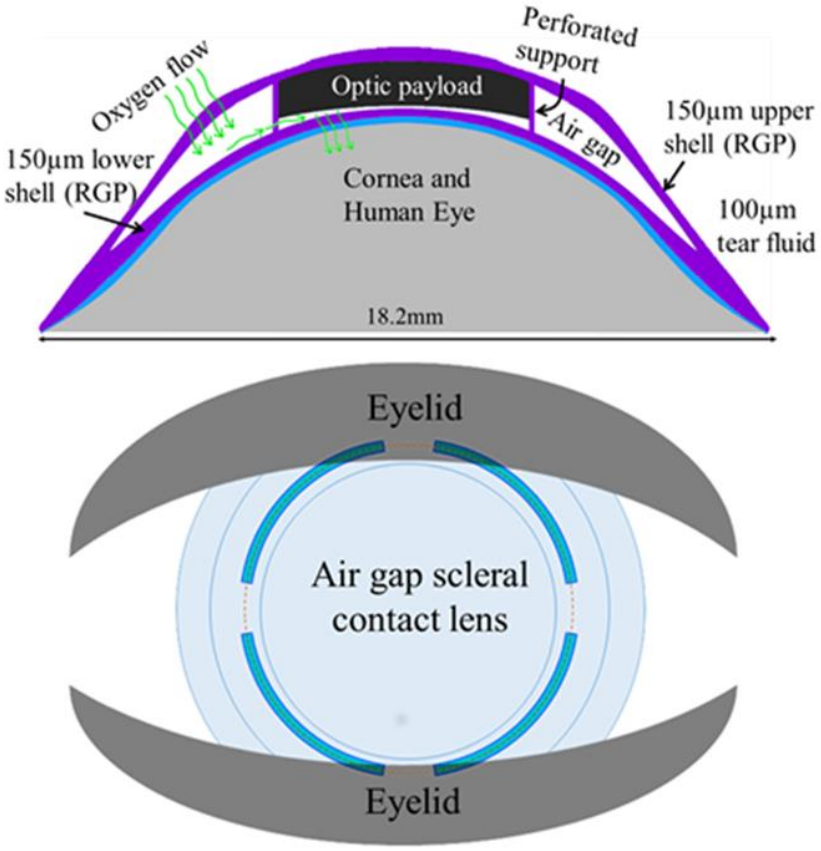

Figure 3-3: Top) Schematic of air-gap solution for providing oxygenation to the cornea, Bottom) geometry of eye with scleral lens, and distribution of fins (4 in this case) along the structural support of the contact lens.

To verify this we conducted simulations in COMSOL of a simplified worst-case model of an eye with a scleral lens and an impermeable "eyelid" partially covering part of the lens (Fig. 4). The model is of an aerated lens with the following features: (1) a circular surface at the center bottom, which is in contact with the cornea; (2) a thin layer of gas-permeable (RGP) material at the bottom (lower shell); (3) a thin cavity above the bottom RGP layer, providing the oxygenation to the cornea; (4) a layer of gas-impermeable material (folded optical elements of the lens) above this central area; (5) gas permeable top layer (upper shell); (6) gas-impermeable outer cylindrical surface (that would not be

present in the future real lens); (7) gas-impermeable ring-shaped outer area at the bottom (the area in contact with the sclera, through which no net flow of O2 occurs in the first approximation); (8) annular void; and (9) RGP partition between the central cylinder and the annular void, forming fins at the bottom. Another key parameter is the O2 permeability of the RGP material of the lens. It is intended to be Paragon HDS®100, which has permeability of ~100×10-11 cm2/s×[mL O2/mL material × mmHg], which for all purposes of our simulation (a steady-state situation) is equivalent to a combination of 100% solubility (the same as in the gas phase) and a diffusion coefficient of 0.76×10-6 cm2/s. The O2 transport is from the atmosphere through the outer ring-shaped region of the upper shell (above the annular void), through the annular void region (8), towards the thin air cavity (3) and from the air cavity through the lower shell (2) towards the cornea (1). The simulation results indicate a nearly uniform distribution of the O2 concentration over a plane at 30 μm distance from the bottom surface of the lens in the 11mm diameter circle just above the cornea, other than in the immediate vicinity of the fin. The ~0.090 value of the O2 concentration at the 30μm distance suggests that the transport of O2 towards the bottom of the lens (cornea) is equivalent to the O2 transport though a uniform layer of the solid RGP material with a thickness of 30 μm/0.090 = 333 μm. Such layer of HDS®100 is thin enough and consistent with common contact lens practice to ensure sufficient oxygenation of the cornea.

Azimuthal variations of the O2 concentration are minimal as well, suggesting that it is sufficient to have just four openings connecting the annular void with the thin cavity above the cornea. Using a larger number of openings would further improve the azimuthal uniformity. We also performed 2D numerical simulations to account for changes in the O2

transport due to fins (made of the same RGP material) that may be introduced into the thin cavity to make it more structurally stable (Fig. (4b)). An actual fin will have a finite length. Therefore, the 2D simulation is the worst-case scenario for the reduction in the O2 transport. A proxy for the O2 transport rate is the O2 concentration at a given short distance above the bottom of the lower shell (10 μm). The simulation indicates maximal reductions of the local transport rate by 5%, 11%, 17.5%, 25%, and 37% for 100, 150, 200, 250, and 300μm wide fins, respectively. So, for example, adding a 250 μm wide fin in an internal area of the thin cavity in the lens will reduce the local O2 transport under the center-line of the fin to a rate equivalent to that through a uniform 400μm thick slab of RGP.

These calculations indicate the potential effectiveness of this structure to provide oxygen, and the introduction of a thin internal air gap on the optical functionality has a negligible impact on optical performance, as will be demonstrated in the following section. This fabrication of this structure is, however, a significant technical challenge. A research effort on this topic is under way, and will be reported separately. For the remainder of this paper, we will concentrate on the design and prototyping of the lens structure compatible with the air gap oxygenation for extended wear, and with a solid lens structure for short term clinical evaluation of performance.

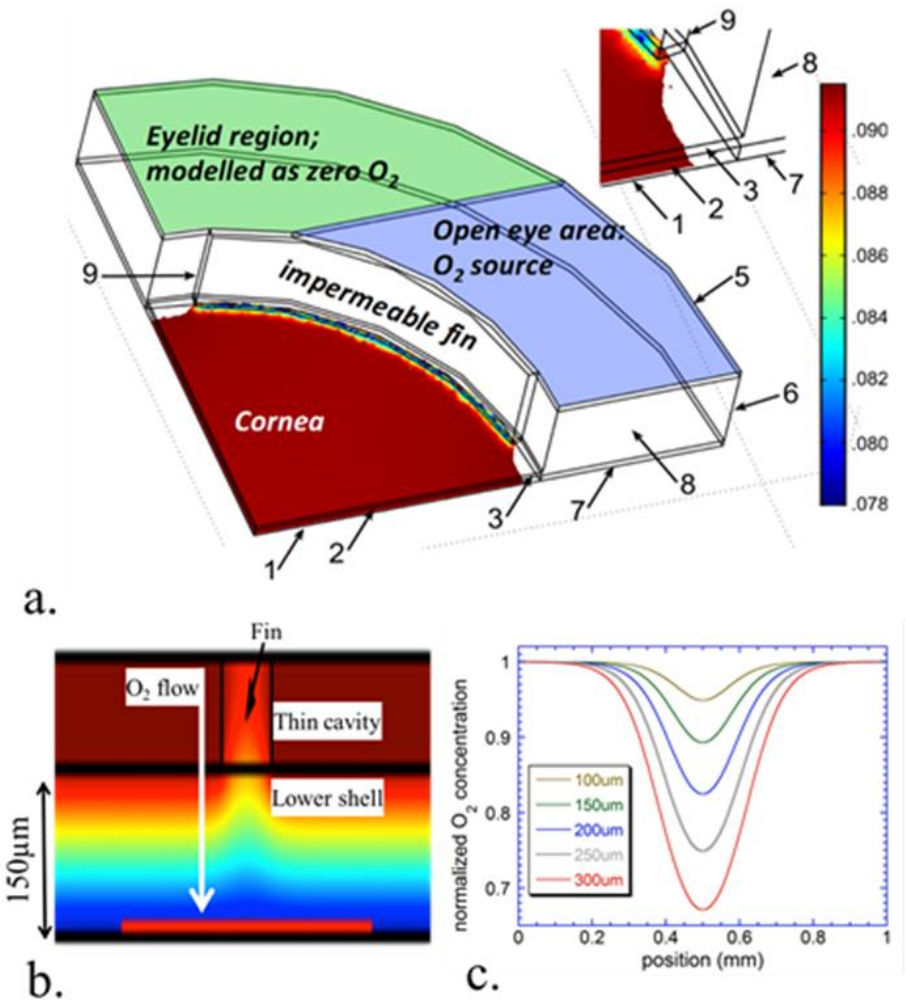

Figure 3-4: a) 3D COMSOL model of simplified air-gap geometry, b) 2D model of air diffusion across perforated gap to the lower shell of the contact lens, c) normalized concentration of oxygen depending on cavity width.

3.2.2 **Optical design**

The key difference between the contact lens telescopes and the previous work on 4- and 8-reflection imaging lenses is that the imagers used a substantially planar front surface, while the contact lens input aperture must follow the curvature of the eye's surface. This is important for the optical design the initial refraction at the lens input introduces

color-dependent optical power, whereas the subsequent internal reflections are intrinsically wavelength independent. No combination of simple mirrors can correct for the significant initial chromatic aberration introduced by the curved input face. The Gen 0 telescope (Figs. 1 and 2) used a surface relief diffractive kinoform structure to correct this axial color, but such a structure cannot be used with a wearable lens. Tears from the eye would form a tear film over the lens, smoothing the diffractive surface to reduce both diffraction efficiency and the chromatic correction, and the surface relief structure would also cause discomfort for the wearer when blinking. The diffractive kinoform in the PMMA substrate can be hidden below a covering layer of index ncover, but this would require increasing the depth of the features from $\lambda/(nPMMA-1) = \sim 1\mu m$ to $\lambda/(nPMMA-ncover) = \sim 10\mu m$, increasing the usable lateral feature size above the length required for color correction. It could also be fabricated on the first reflective surface, which would require the depth of the multi-level or analog features be reduced to $\lambda/2nPMMA = \sim 0.1\mu m$, which would require excessive precision in the step size.

Instead, the wearable lens we investigated uses refractive color correction by a combination of PMMA "crown" (n=1.49, Abbe number 58) and Paragon's HI-154 rigid gas permeable contact lens material, which has a high refractive index and relatively high dispersion (n = 1.54, Abbe number 29), acting as our "flint". The optical design of the new lens is shown in Figure 5. This lens is designed using the immersed fused silica elements and curved focal surface of our model eye (as in Fig, 1), which will be described in Section 4.1, including Fig. 11, and reference [41]. The normal 1x vision path through the 2.6mm diameter (21.2mm2 area) central circular aperture provides F/# 4.1 vision. The 2.8x magnified vision path through the annular input with 4.1mm outer and 2.78mm inner radius

(28.5mm2 in area), providing F/# 9.7 vision. The four reflections introduce additional loss on the telescopic path, so the T/# for this path can be higher, depending on fabricated mirror reflectivity. The central path uses substantially spherical surfaces, with a small even aspheric correction. The annular telescopic path relies on high order aspheres to correct for optical aberrations in a limited optical path length. The prescription of the scleral lens can be modified for any user by adjusting the power of the input surfaces for the 1x and 2.8x paths, including spherical power to correct for myopia or hyperopia, and cylindrical power to correct for astigmatism.

In the fabrication process used to make the first "GEN-1" lens, areas between and around the annular rear mirrors were also mirror coated, creating some reflective non-optical surfaces. Reflections from these surfaces do not enter the eye, but these surfaces do block off-axis light (Fig. 6(a)). All light from the object scene needed to pass through the 1x aperture, and axial offset of the 2.6mm entrance aperture from the internal pupil of the eye caused considerable vignetting of the 1x vision path. The fabrication process used in a second fabrication of a "Gen 2" optic (as described in the following section) was revised to increase the field of view of the 1x path. This removed the unnecessary mirrors and filled the regions with a material of the same refractive index as the PMMA substrate for the folded optic, providing unaberrated pathways for peripheral vision, as shown in Fig. 6(b).

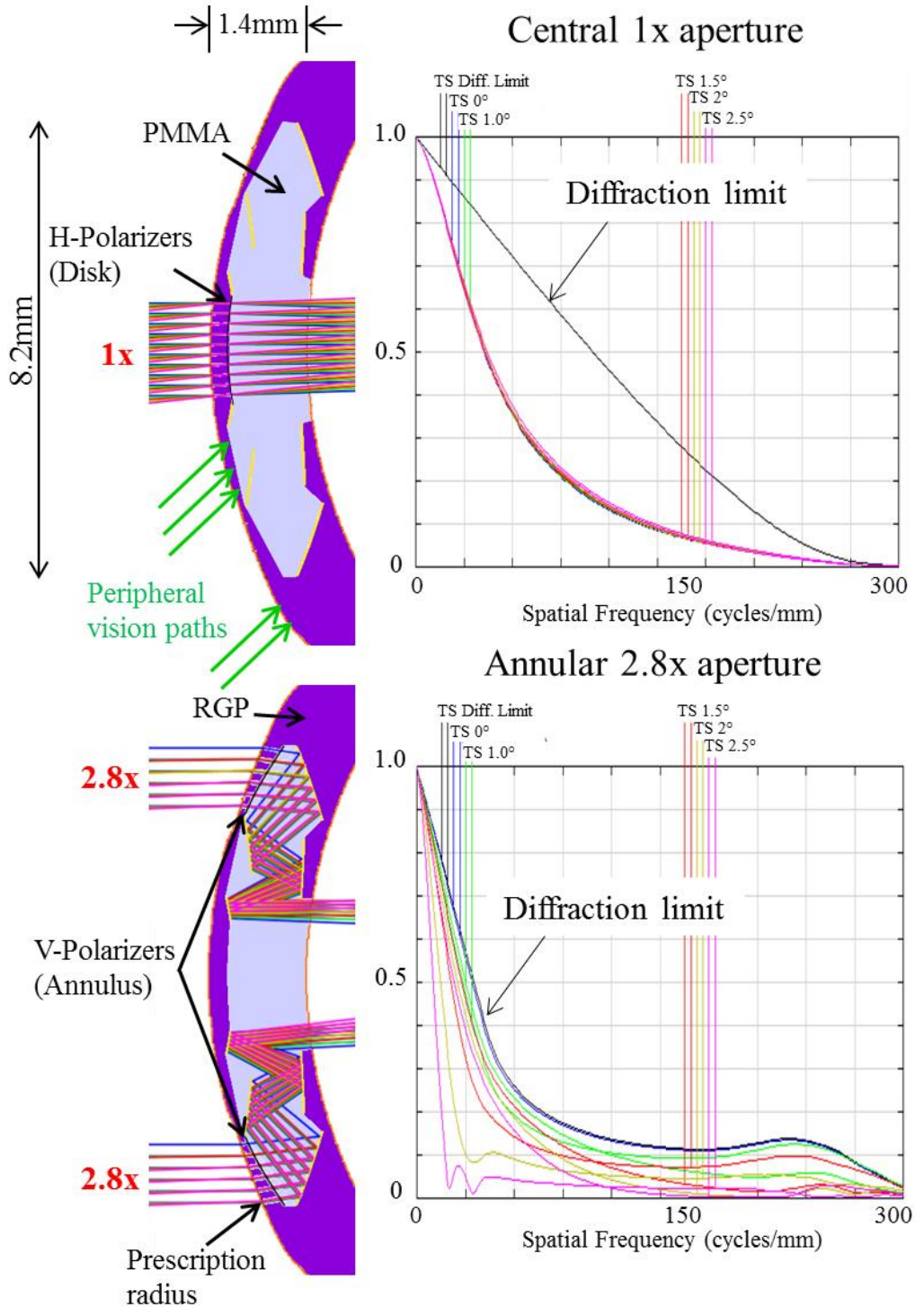

Figure 3-5: Schematics of the scleral contact lens with polychromatic MTF calculations on a model eye with a pupil of 4mm for (Top) 1x unmagnified vision, and (Bottom) 2.8x telescopic vision.

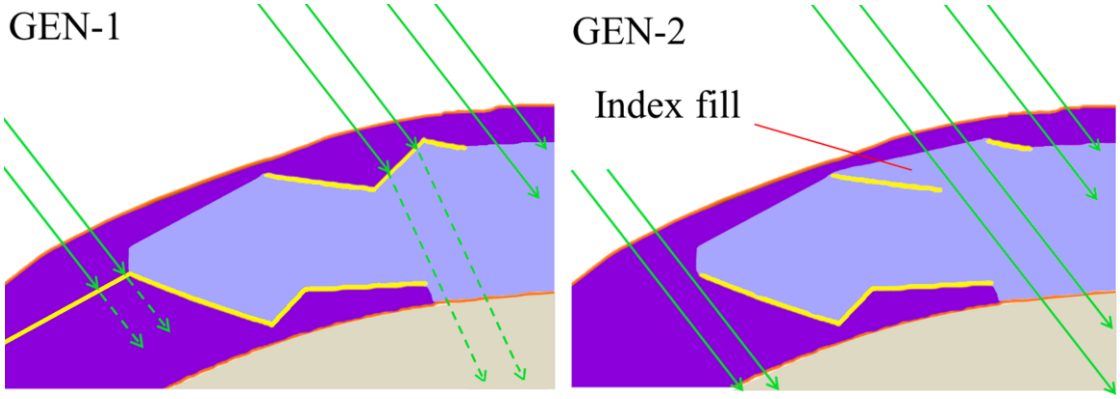

Figure 3-6: Left) Close up of GEN-1 scleral lens, Right) Close up of GEN-2 scleral lens.

3.3 Fabrication and assembly process

In this section we concentrate on the fabrication and test of a lens for short term wear. Figure 7 shows the components and assembly steps for the GEN-2 switchable telescopic scleral lens. The center of the lens is a PMMA diamond turned insert (”precision telescope insert”) with enhanced aluminum coated annular mirrors. This element was fabricated by ISP optics using a 250UPL single-point diamond lathe. This part needs to be surrounded by complimentary-shaped PMMA and HI-154 index fills. The telescope insert is placed between a top PMMA index fill and a bottom HI-154 index fill diamond turned by Paragon Vision Sciences using an Optoform 40 ophthalmic lathe, forming a solid cylindrical “triple stack.” The parts were bonded by Dymax 141-M, a flexible medical UV-cure adhesive with refractive index 1.49, similar to the index of PMMA. This stack is then diamond turned to a “shaped post,” where the only part of the top index fill that remains is a thin layer between the top two annular mirrors. This volume is necessary to avoid distortion of the peripheral vision path.

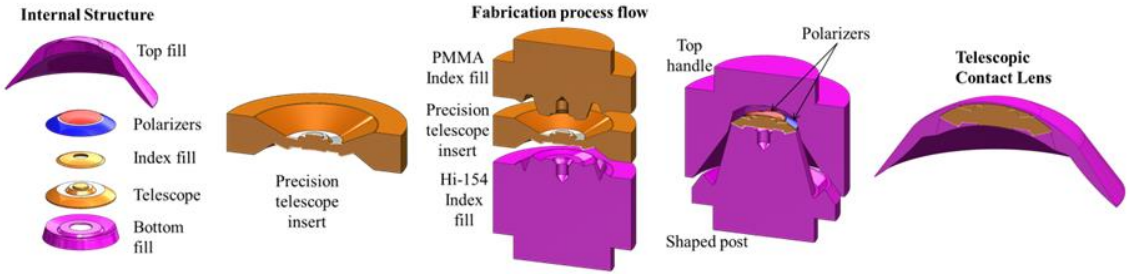

Figure 3-7: Left to right: Components for scleral contact lens, diamond turned PMMA and aluminum coated precision telescope, triple stack to form index fill for peripheral region, post cut for polarizer attachment and RGP shells, final telescopic contact lens.

In a future assembly process, two orthogonal polarizers that cover the unmagnified and telescopic vision paths will be bonded to the shaped-post surface to enable a polarization-based switching mechanism. A top handle composed of HI-154 is then bonded to the shaped-post using Dymax 210CTH, a more rigid medical UV cure adhesive, imbedding the index filled telescope between two high refractive index parts that provide achromatic correction and the overall scleral lens shape. Finally, this part is diamond turned into the scleral lens, based on the wearer's physical and optical prescription. Figure 8(a) and 8(b) show the triple stack components prior to bonding, and the post cut, including the PMMA index fill. Figure 8(c) and 8(d) show the completed scleral lens where the annular rings appear to be “floating” in the PMMA medium, where the transparent spaces between the mirrors provide the peripheral vision path. The completed optic is 18.2mm in diameter, with a center thickness of 1.6mm. Figure 9 shows a cross-section of one of the completed lenses, revealing the glue line thicknesses and the quality of the match between the insert and the HI-154 material. The adhesive seam is uniform over the input aperture, with a 35µm thickness determined by the uncured adhesive's viscosity and the physical match

between the shaped parts, which are designed to come in contact at the shoulders outside the input aperture.

We measured the dimensions and profiles of the insert and contact lens to determine if there were any of significant deviations from the intended design. ISP provided an inspection report of the surface roughness for the optical annular regions to be less than 6nm; however these measurements were conducted prior to the mirror coating. A white light interferometer scan revealed a roughness (Ra) of 12nm for the aluminum coated regions, and an Ra of 23nm for the air-to-polymer interface at the input of the telescopic path. Figure 10 shows a color map of a regional scan of both the insert and the 2.8x input surface.

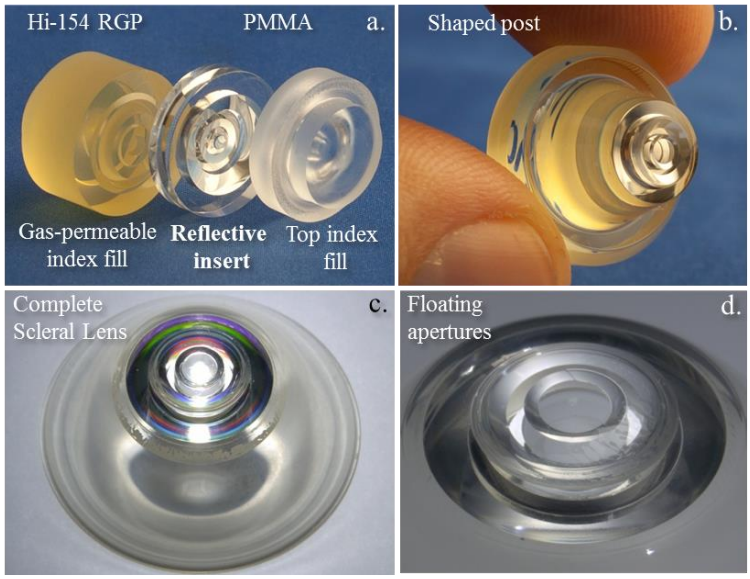

Figure 3-8: a) Unassembled triple stack of scleral lens components, b) cut post with PMMA index fills, c) complete scleral lens, d) close up of floating apertures for peripheral region.

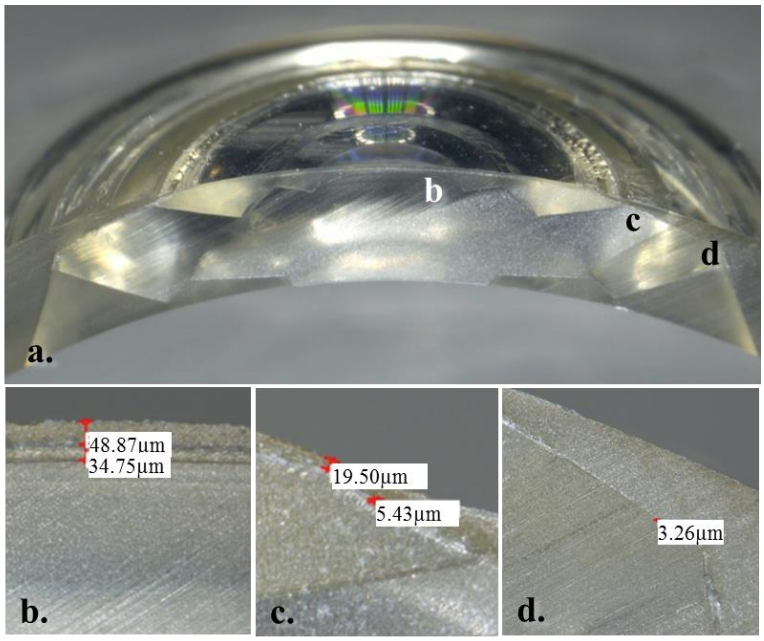

Figure 3-9: Cross-section and glue line thickness of scleral lens.

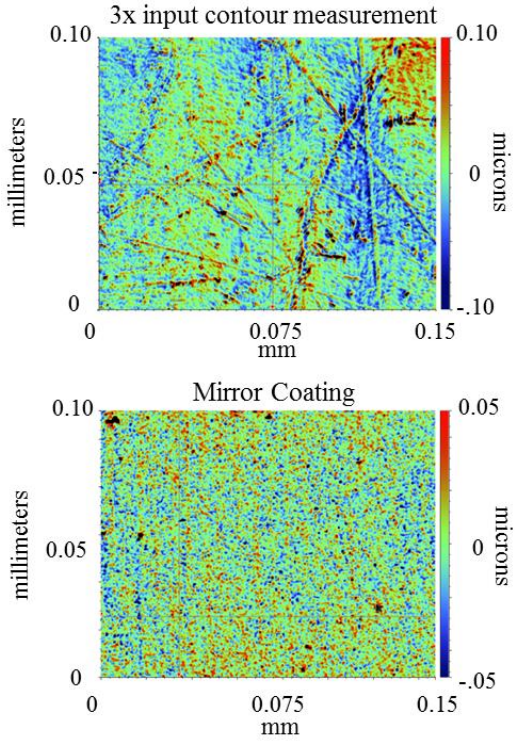

Figure 3-10: Fig. 8: Veeco white light interferometer scan of (Top) ISP mirror coated insert, and (Bottom) HFZ 3x input surface.

3.4 Testing of scleral lens

3.4.1 Imaging performance

The resolution of the telescopic scleral lens was measured using an optomechanical fluid filled eye model with a full field of view of 34° (Fig. 11) [41]. The design of the eye model optics was derived from the Navarro eye model, with fused silica single elements with conic surfaces for both the cornea and crystalline lenses. Distilled water fills the regions between the 1.458 index lenses to replicate the aqueous and vitreous humors of the human eye. The imaging surface is a fiber bundle that transmits the focused object scene from the curved input face to the planar output where the image is emitted into free space, and then photographed using relay optics and a Canon DSLR camera.The scleral lens is placed on the cornea of the eye model with distilled water and is held in place by surface tension. Figure 11(b) shows circular and annular apertures positioned in front of the scleral lens and alternated to enable switching between normal and telescopic vision. The object scene was placed approximately 6 meters away from the testing apparatus, and images were captured for both the 1x and 2.8x path. The eye model is focused by moving the curved-face fiber bundle along the optical axis to the optimum position for the telescopic path.

Figure 12 shows images acquired of the 1x and 2.8x telescopic path, where the eye was focused to obtain the best 2.8x image. The on-axis MTF of the optical system (Fig. 13) was measured using a slant-edge pattern and Imatest software .Resolution for the telescopic path was significantly lower than the theoretical design (Fig. 5), with an average horizontal and vertical MTF10 of 13 cycles/mm. The drop in 2.8x path resolution will be discussed further in Section 5. The resolution of unmagnified vision path has also dropped

by comparison to the bare eye model [41], as the best focus for the telescopic vision path was approximately 100µm away from the 1x vision best focus. Focusing for the unmagnified vision path achieves an MTF10 of 103 cycles/mm, or 20/20 equivalent vision, according to design.

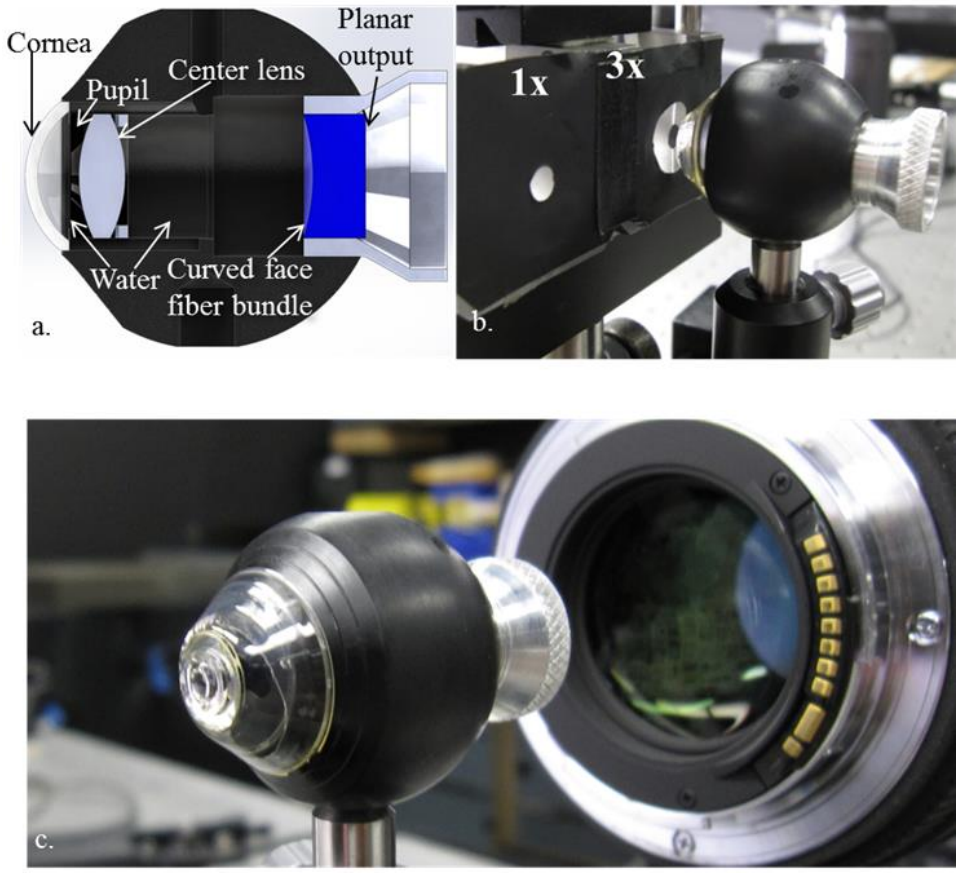

Figure 3-11: CAD cross section of testing apparatus for HFZ lens, b) switching between 1x and 2.8x vision, c) Relay imaged to camera.

Figure 3-12: Image results of HFZ lens on eye model. (Top) 1x path and (Bottom) 2.8x path.

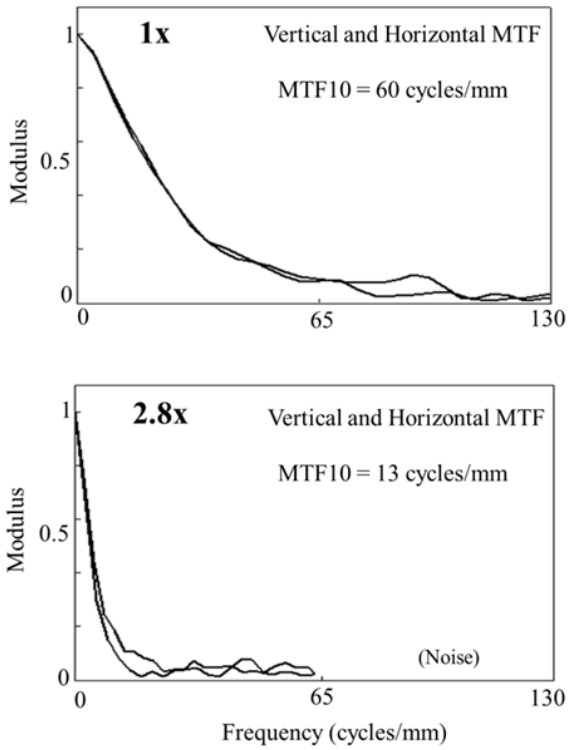

Figure 3-13: Vertical and Horizontal MTF measurements for both (Top) 1x path and (Bottom) 2.8x path.

3.4.2 **Peripheral vision testing**

The 34° field of view of the eye model covers a region larger than the fovea, but is inadequate for testing the peripheral vision. A simplified optical system that approximates the focal length and F/# of the eye was used to quantify the transmission of light through the peripheral vision paths as a function of angle (Fig. 14). The GEN-1 and GEN-2 lenses were positioned in front of a biconvex lens with a focal length (18mm) (nearly equivalent to the human eye) and an aperture of 4mm (similar to the nominal pupil size) The distance between the scleral lenses and the biconvex lens was approximately 4.5 mm, to replicate the anterior chamber depth (ACD) of the eye. A 5 megapixel CMOS imager was placed at

the focal point of the system and measured the intensity of the transmitted light which could pass through the 1x aperture, through the peripheral index matched regions (between the annular reflectors), and through the edge of the scleral lens' skirt (Fig 14(b)). The normalized transmission intensity as a function of angle was measured by varying both the angle of illumination of the white light source and the position of the sensor. Figure 14 shows that the GEN-1 contact lens non-optical mirrored regions prevented the transmission of light at large angles, limiting peripheral vision to well below 30°. However, the floating annular mirrors and PMMA index filled regions of the GEN-2 lens allow for light

transmission at larger angles, providing peripheral vision up to 55°, nearly doubling the field of view of the GEN-1 design.

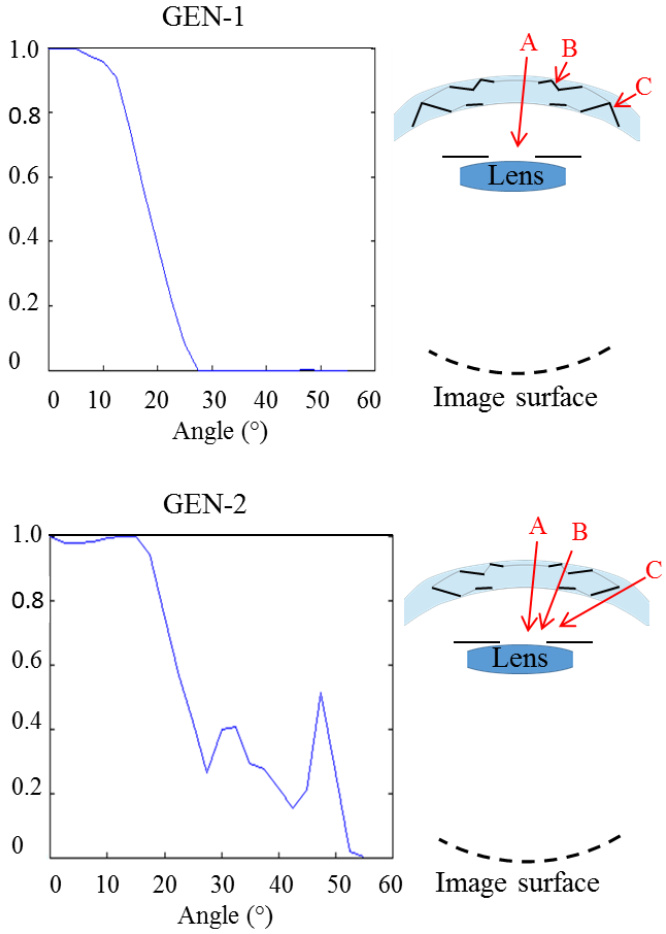

Figure 3-14:Measurement of the transmission of the peripheral path in (Top) GEN-1 contact lens, and (Bottom) Gen 2 contact lens.

3.5 Limitations to resolution

The measured resolution of the 2.8x path, while well below the design, is at a level which may be useful as a low vision aid for AMD patients. However, the resolution may be primarily constrained by the final fabrication step, the shaping of the outer lens surface to the wearer prescription. This step was done by the Optoform 40 diamond turning, using

processes that are standard for scleral contact lens manufacturing. However, the 2.8 magnification of the folded optic is more sensitive to fabrication errors, including surface roughness. Measuring a larger region of the air-polymer telescopic path's input surface revealed an (Ra) = 23nm with peak-to-valleys of 150nm (Fig. 15). The roughness of the surface profile for the telescopic path was approximated by integrating along the arrowed line on the measured surface plot, followed by tiling the measurement a total of 4 times in series from one another. This approximated roughness profile was used to modulate the designed input surface calculate the MTF of the roughened surface, and is shown by the red line in Fig. 16. For the roughness by a factor of 1/5th and observed an improvement in the system's MTF. Therefore, we believe that the drop in resolution is caused by surface roughness of both the input surface of the scleral lens and the mirror coating on the diamond turned insert. The performance of the system can possibly be improved by switching to higher precision diamond turning technology. Standard commercial contact lens equipment can rapidly fabricate contact lenses for custom prescriptions with accuracies sufficient for

conventional vision correction. However, a higher performance telescopic lens may require advanced diamond turning (or post polishing) for the final lens shaping.

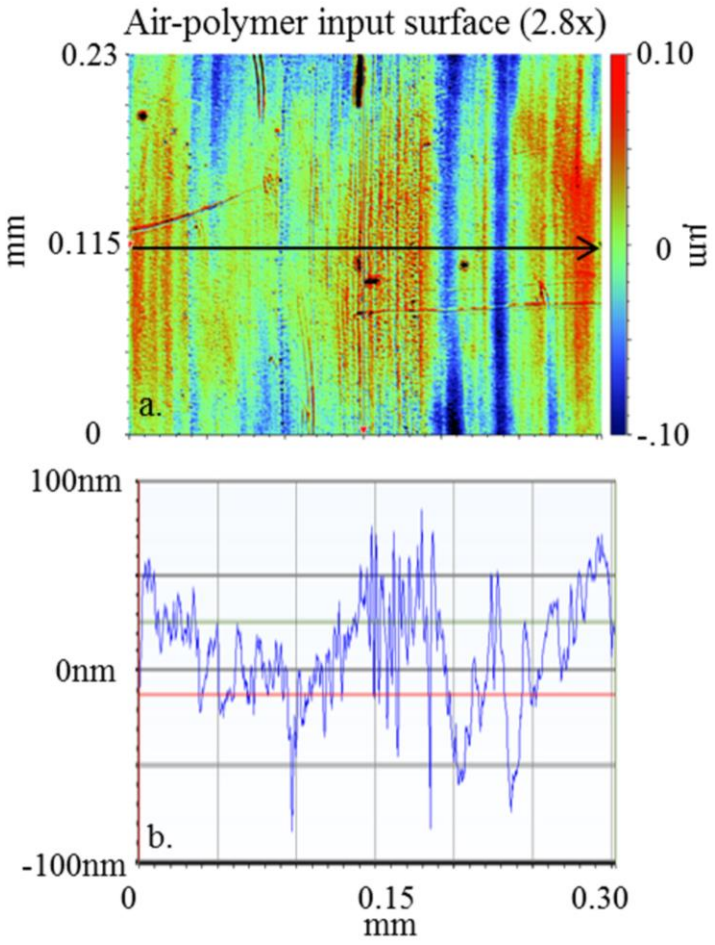

Figure 3-15: Top) Veeco white light interferometer regional 2D measurement of 2.8x path, Bottom) line profile across 2D scan.

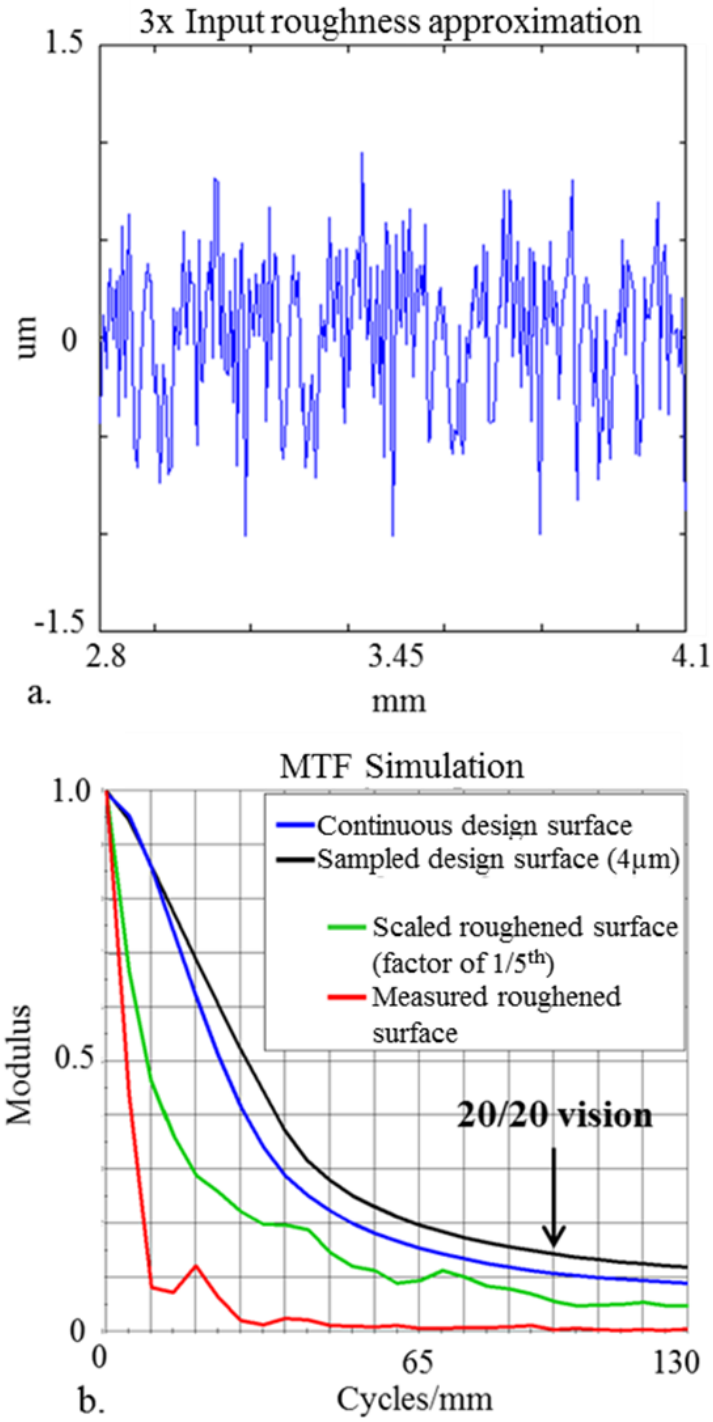

Figure 3-16: Top) Approximation of surface roughness across 3 profile from Veeco interferometer scan, Bottom) FRED MTF calculation for roughened 2.8x path surface profile.

3.6 Clinical test

An Investigational Review Board approved clinical study was conducted on a single eye of five adult subjects. The clinical supplies were the telescopic-only GEN-1 scleral lens. The lenses did not have the mechanism for providing oxygen to the cornea. As a result, the subjects wore the contact lens for a short period of time (~30min). The investigational lenses were measured and found to not have optics that were reduced in quality due to mirror adhesion and surface roughness. A decision was made to proceed in an effort to measure the centration, movement, comfort and presence or absence of magnification.

The lenses were applied (Fig. 17), and allowed to equilibrate for 15 minutes. The lenses demonstrated centration horizontally and an average of 0.5 mm displacement below the geometric center of the pupil. The lenses were stable and were observed to have less than 0.2 mm movement on the blink. All subjects reported the lens comfort to be good or very good. As expected, the subjects reported their vison to be blurred, but reported magnification when comparing the image size with the contact lens to that of their eye without the contact lens.

The results from this small exposure sample with the non-optimized optics and absence of the oxygen mechanism support the feasibility of the scleral lens platform to deliver a well centered, stable and comfortable form factor for telescopic magnification.

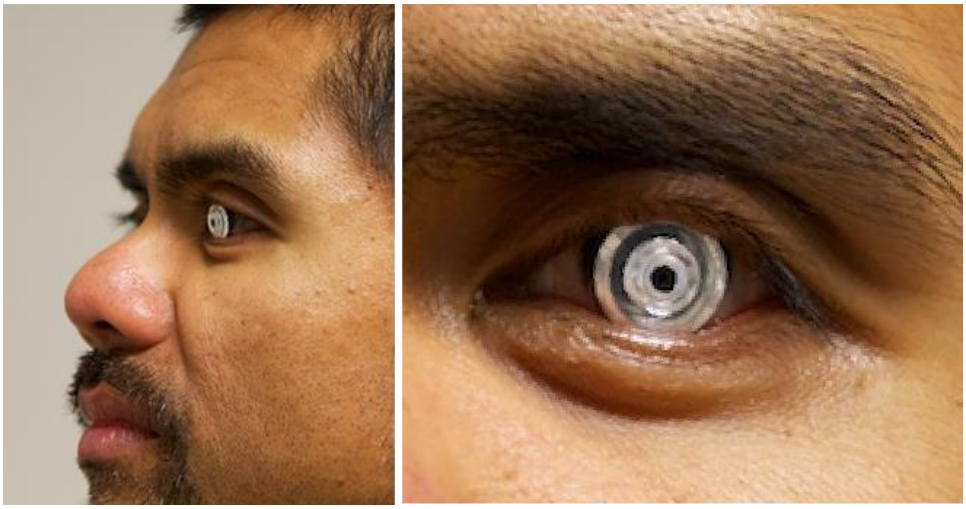

Figure 3-17: Test subject wearing the GEN-1 contact lens

3.7 Chapter summary

In conclusion, we have shown the optical design and fabrication of a wearable eye-borne telescope in the form of a scleral contact lens. The lens was tested in the laboratory using a life-sized model eye, and shown to image both 1x and 2.8x vision paths. We show modeling results that indicate that the 2.8x path resolution was limited by fabrication tolerances, most notable the surface finish on the input aperture. This surface finish may be improved using higher precision diamond turning, or by post-polishing of the lens surface. An initial form of the lens was tested in a small scale clinical demonstration on human subjects. This initial lens was oxygen impermeable, and oxygen delivery to the cornea is a subject of further research and development. We described two methods that can lead to an extended wear version of the lens. Another subject of ongoing work is the integration of spatially patterned polarizers to distinguish between 1x and 2.8x vision paths, as well as self-contained polarization switching eyewear that will allow hands-free switching between magnifications.

Chapter 3 is entirely a reprint of the material as it will appear in “Wearable telescopic contact lens,” by A. Arianpour, G.M. Schuster, E. Tremblay, I. Stamenov, A. Groisman, J. Legerton, W. Meyers, G. Alonso, and J.E. Ford, Applied Optics (2015).

4. Enhanced signal coupling in wide field fiber-coupled imagers

4.1 Introduction

Fiber-bundle imaging has a long history, including medical applications like endoscopy and laparoscopy, where fiber bundles transport a remote image plane for detection or viewing [43]. Imaging fiber bundles can also couple light between non-planar image surfaces, including the spherically curved image formed by "monocentric" hemispherical objective lenses [44,45]. Conventional wide-angle lenses, especially extreme “fisheye” lenses, increase field of view at a cost in light collection relative to their large input aperture and volume, producing distorted and relatively low-resolution planar images. Using spherical optical surfaces eliminates the most problematic geometrical aberrations and potentially allows high-resolution wide angle imaging. Deeply curved image sensors cannot be fabricated using conventional semiconductor wafer processing, but a fiber bundle can connect a planar sensor to the spherical image surface. Such an imager was first made by Lawrence Livermore Labs [46]. Light incident on a curved input surface of numerical aperture 1 fiber was coupled into a dense array of straight N.A. 1 fibers, and then transmitted to a flat output surface connected to a 576x384 pixel CCD focal plane. However, the Clementine “Star Tracker” [47] had only a

52˚ field of view, which took little advantage of the potential of the monocentric lens configuration. The field of view limitation of the single-sensor Clementine star tracker came from refraction at the input face of the curved fiber bundle. For a flat NA = 1 fiber, light couples for angles ranging from 0° to 90°. In a curved-face fiber bundle, light in general is incident on an angled facet. Figure 1 shows that at some angles the refracted light can exceed the internal critical angle resulting in high loss, and the transmitted signal may reflect from the output face of the fiber, or emit into such a large angle to interfere with focal plane sensing. A finite thickness between the bundle and the sensor prevents the fiber bundle from making direct contact with the active region of a sensor. Given this physical gap, the divergence of light can potentially overlap multiple pixels in the sensor, effectively blurring the impulse response and reducing resolution.

We modeled a F/2 nearly diffraction-limited monocentric lens system and fiber array (NA = 1, n_{core} = 1.81, $n_{cladding}$ = 1.48) using Photon Engineering's FRED non-sequential ray trace software, calculating the coupling efficiency through a 3x3 fiber array positioned at different field angles. The coupling efficiency as a function of field angle for the system seen in Fig. 2. A significant drop in intensity is observed as the fields approach the complement to the critical angle of the system (35° with respect to the fiber's axis) and a negligible amount of power couples into the fibers beyond that point. Both coupling efficiency and divergence between the fiber bundle and focal plane sensor means that a wide emission angle causes a broadening in the point spread function. Therefore, these fiber coupling effects must be addressed to make effective use of the principle performance advantage of the monocentric objective lens, so that it can maintain high-resolution over a wide field of view.

.

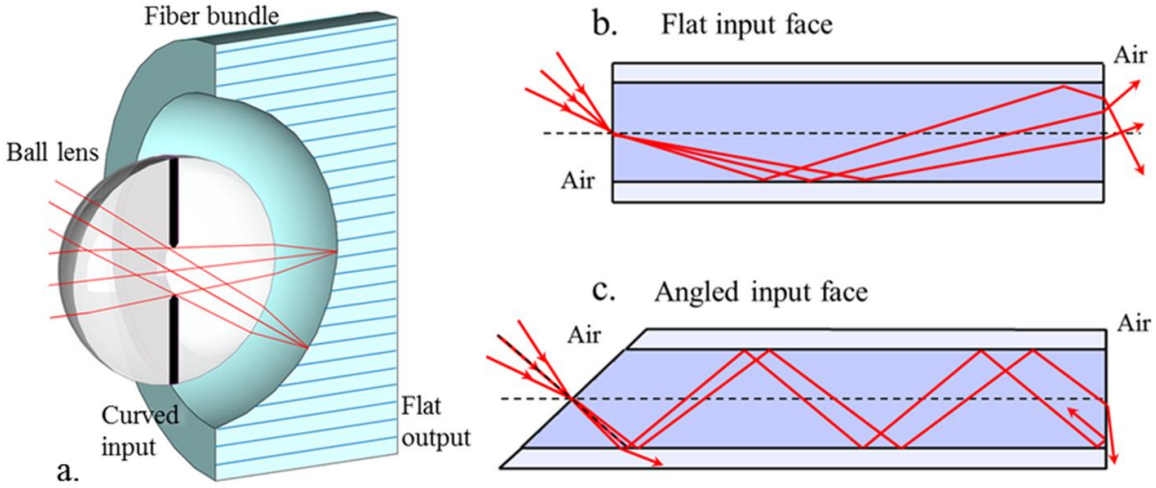

Figure 4-1: a) 3D geometrical schematic of monocentric fiber coupled imager, b) shows how an off-axis focusing beam would couple into a fiber bundle with a planar face, while c) shows how the locally angled input face of the curved-face fiber bundle interferes with signal coupling, and limits the maximum angle achievable with a simple straight fiber bundle.

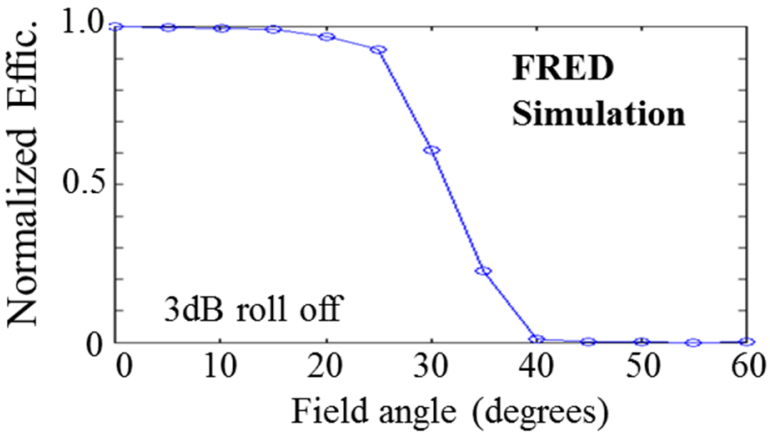

Figure 4-2: FRED simulation of coupling efficiency of an F/2 nearly diffraction limited monocentric lens with 2.5µm pitch fibers. The power drops off dramatically as the field approaches the 35˚, the complement to the critical angle of the fiber bundle.

Recently, we demonstrated a compact 30 Megapixel monocentric imager with a 120˚ field of view using multiple fiber-coupled CMOS image sensors [48,49]. The imager divides a single image surface into 6 sections, with curved face fiber bundles closely tiled

across the curved image surface. The sensors are arranged such that each section covered less than 30˚ diagonal angle, and so they maintain good illumination uniformity. One difficulty with this approach is the fabrication and mechanical alignment between the bundles; even a small gap causes loss of image data. Another alternative is to use a fully 3-dimensional waveguide array. If the fibers are internally curved so that the input fiber axis is close to normal to the focused light beam, and the output fiber axis is close to normal to the focal plane sensor, then the incident light is efficiently coupled and the propagating light mode adiabatically transformed to a desirable emission and efficiency coupling to the focal plane sensor [48,49]. This solution can potentially enhance the coupling efficiency for a wide range of angles, but the fabrication of the required 3-D waveguide structure is more challenging than of the straight fiber bundles. Recently, research groups have used tapered fiber bundles with flat input and output surfaces for relay imaging and demagnifying the size of the image, but do not use a curved input surface or monocentric lens for reducing the optical components [50].

A different approach to enable coupling of a wide range of incident angle light into a straight fiber bundle is to modify the beam incidence angle just before it is incident on the fiber face. The challenge is to create a structure near the interface of the input fiber that can either refract or diffract the focusing beam at angles to increase the coupling efficiency and reduce the divergence angle for a single curved-face fiber bundle. As Fig. 3(c) shows, this structure can be located at or before the spherical image surface. A deflector located at the image surface may or may not maintain spatial wavefront coherence. For example, a diffuse scattering surface such as a roughened fiber input face will send at least some of the incident light into guided modes. We experimentally tested this approach, but found it

provided only a slight enhancement in wide-angle signal coupling, and a negligible reduction in the divergence of the exiting beam. As an alternative, a radial beam deflector at or near the image plane that maintains spatial coherence of the focusing wavefront can increase coupling efficiency and also can be adjusted to reduce the divergence at the output of the fiber. Such a beam deflector can be refractive or diffractive. A refractive surface (e.g., microprism) offers a broad spectral response, and may potentially be manufactured at low cost by embossing or molded onto the curved surface. This method is preferable over the sectioned or 3-D waveguide structure since it uses current manufacturing processes, and can potentially be accomplished at the wafer-level. In this paper, we investigate this approach, and show that a refractive micro-prism array surface can redirect the incoming focusing beam at the extreme angles to improve system coupling efficiency and increase the maximum field of view from approximately 50˚ to 90˚. In Section 2, we compare the response of both flat and curved-face fiber bundles with NA = 1 fibers using both a non-sequential simulation and experimental characterization. In Section 3, we present an analytical solution to design of the blaze angle of the micro-prism array, with an analysis of the effect on system performance. In Section 4, we demonstrate a proof of concept using a monocentric fiber-coupled imager with and without a region of embossed micro-prism array, then conclude in Section 5.

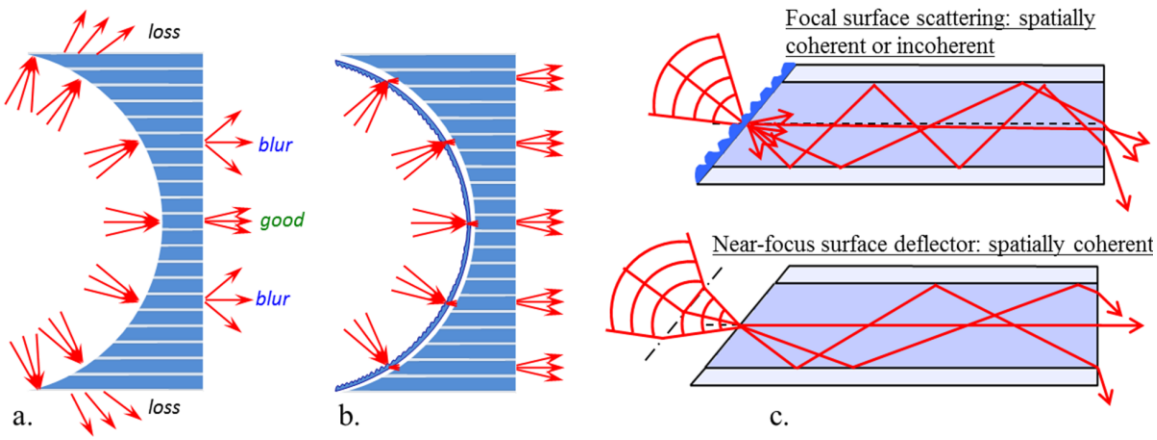

Figure 4-3: Illustration of light coupling into fibers at various angles for a) bare curved-face fiber bundle, b) surface-enhanced curved-face fiber bundle, and c) enlarged view of a scattering facet surface and a beam deflective structure modifying the focusing beam beam to enhance coupling in an angled facet.

4.2 Modeling and characterization of fiber bundles

Examining the difference in divergence angle for the two geometries (flat and curved-face) reveals the system's response in monocentric fiber coupled imaging, and provides metrics for engineering the radial micro-prism array on a curved-face bundle. To begin, we investigated the coupling and emission response of flat and curved-face fiber bundles to an incident collimated beam. In a monocentric imaging system, a cone of light is incident on a curved image surface with the chief ray normal to the imaging surface for all field angles. Substituting a curved-face fiber bundle for an image surface, the chief rays are incident normal to the angled facets of the individual fibers. Evaluating the system with respect to the chief rays approximates the divergence and coupling efficiency for a given F/# imaging system using a curved-face fiber bundle.

Approximating the system using geometrical optics, Fig. 4 shows a FRED non-sequential ray-tracing simulation to view the cross section of the imager, and illustrate the

divergence when exiting the fiber. The source was a monochromatic (532nm) collimated beam for field angles ranging from 0° to 45°. Each field angle was associated with a 3x3 array of cylindrical fibers for both the flat and curved-face geometries. The fiber's core and cladding ratio give a numerical aperture of one, and a pitch of 8μm. For our calculations, we assumed the refractive indices of the fiber core and cladding are 1.81 and 1.48, based on published values for Schott's NA 1 fiber [51]. With these indexes, the critical angle is 54.85° with respect to the fiber side wall surface, or 35.15° with respect to the fiber's axis, which we call the axial critical angle. Placing the origin of the beam at the center of curvature of the curved face fiber bundle in Fig. 4(b) replicates the chief ray in a monocentric imaging system. The exiting beam in Fig. 4(a) is a hollow cone which subtends an angle equal to the incident angle of illumination for a flat fiber bundle. In a geometrical optical model, reflection from internal surfaces of the round fibers causes the propagating beam to retain angle relative to the fiber axis, but lose azimuthal orientation, such that the emitted beam is a hollow cone of light. A more accurate physical model, including diffraction, shows a similar effect even of square fibers, unless the fibers are very large compared to the illuminating wavelength.

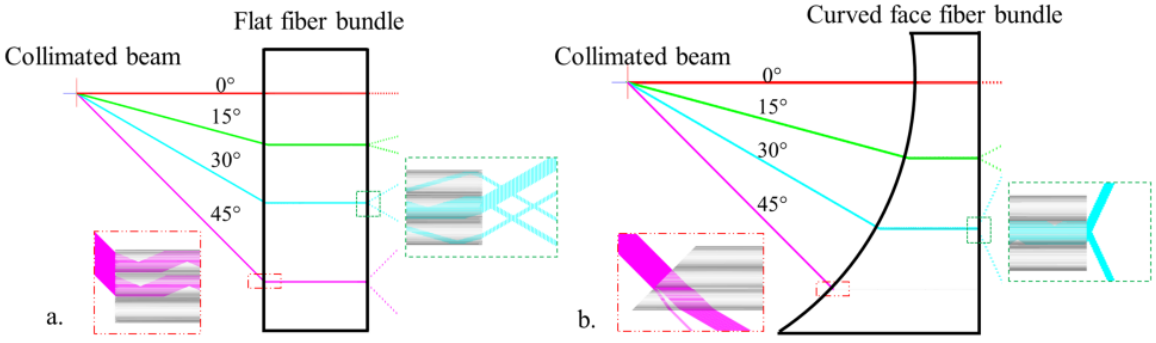

Figure 4-4: FRED 2-dimensional simulation of laser (532nm) incident at 0°, 15°, 30°, 45° incident on a) flat bundle (NA = 1) and b) curved-face bundle (NA = 1) and exiting in air (n = 1).

For the flat-surfaced fiber bundle, shown in Fig. 4(a), rays incident normal to the angled facets refract at the air to fiber interface, and refract again when the light is emitted, returning to the original angle of incidence. For the fiber bundle with a curved input face, shown in Fig. 4(b), the divergence of emitted light increases with angle of incidence upon the curved bundle face. At 45˚, the incident beam is not guided at all. If the illumination angle is larger than the axial critical angle (35° for the given core/cladding combination), total internal reflection no longer occurs, and the beam of light is refracted into the cladding and is no longer transmitted out of the corresponding core. A cross-sectional view as shown in Fig. 4 can be somewhat misleading. The physical structure in the fiber-coupled imager is three- dimensional, and the fibers are approximately cylindrical rods that will couple a portion of skew rays dependent on the angle entering the fiber, but the power coupled is significantly less than the rays close to the fiber axis [52].

We constructed an experimental test to match as closely as possible this simulation, using a plane-plane polished fiber bundle with 7-8μm pitch fibers, and a spherically curved 17.8mm radius input face bundle with 7-8μm pitch fibers, where both bundles were NA = 1. A 532nm laser with a Gaussian beam profile and spot size diameter of 1mm was incident on the input surfaces of the bundles at angles ranging from 0° to 45°. The experimental arrangement and measurement results are shown in Fig. 5. As the illumination angle nears the axial critical angle the coupled light approaches a divergence angle in air of 90°. To reduce the divergence angle, the output surface of the fiber bundle was bonded to a PMMA block (n = 1.49) with a diffusive rear surface. The intensity pattern on the rear surface was imaged with a limited numerical aperture DSLR camera with a CMOS sensor. Knowing the thickness of the PMMA block and the physical size of the image, we measured the

relative intensity distribution across the scattering surface by integrating radially across the image and calculated the power distribution as a function of the angle for the beam as emitted directly from the fiber surface into air. Graphs in Fig. 5 depict the power distribution across the scene with relative peak intensities corresponding to the angle of divergence for all range of angles regarding both fiber bundles. Fig. 5 shows that the flat fiber bundle couples light from 0° to 45° degrees with the peak energy distribution corresponding to the input angle of the respective beam. Most of the energy emitted from both bundles resided in the ring pattern, with negligible energy close to the center of the image except for near-normal incidence light. Light exiting the curved-face bundle diverged significantly as the angle of the input beam increases. The characteristic ring-pattern was not visible at 45˚, and the signal power has dropped to near zero. The injection angle exceeded the axial critical angle of the fiber and significantly reduced the transmitted power at 45°. The number of fibers illuminated changes with the injection angle, but this has minimal impact on the emitted beam divergence.

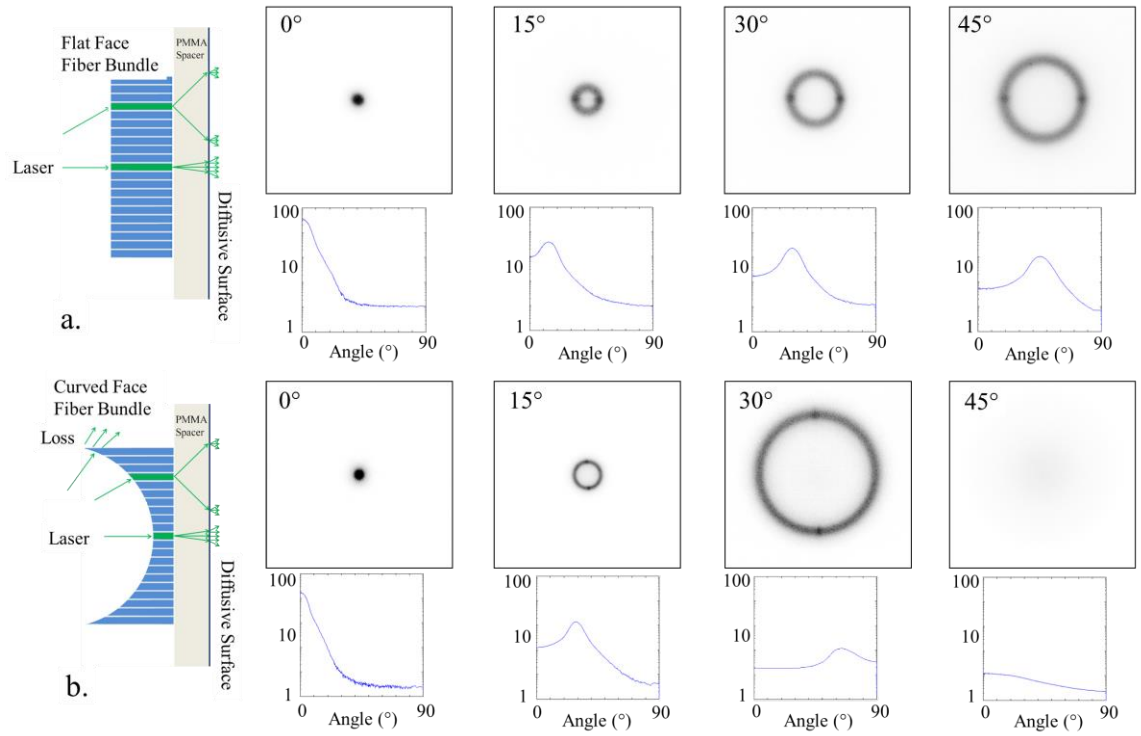

Figure 4-5: Experimental demonstration of a 1mm spot size laser incident at angles of 0°, 15°, 30°, 45° on a) flat fiber bundle, b) curved-face fiber bundle. The contrast of these images have been inverted to show the regions of the dark rings where the intensity is greatest. The exit angles are measured by examining the peak relative intensities for their respective graphs below.

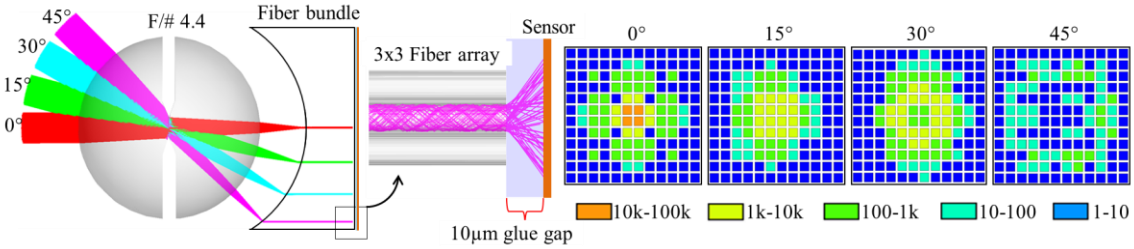

Figure 4-6: FRED Simulation of fiber coupled monocentric imager's output response when coupled to a sensor with a 3.3µm pitch and 10µm glue thickness. The irradiance drops as a function of angle, and at 45° a negligible amount of energy is transmitted to the sensor.

and the incident light is a 532nm collimated source. As in our previous simulations, the fibers are NA = 1 with a core index of 1.81 and cladding of 1.48. Similar to the simpler collimated beam model results, as the field of view widens the size of the point spread function increases and the integrated intensity distribution across the detector decreases.

The blurring due to the gap between the fiber bundle and sensor may be reduced; in fact the most recent experimental fiber-coupled image sensors had a physical adhesive layer which was approximately 5 μm thick [49]. But the loss in intensity when the field angles pass the axial critical angle is independent of the physical gap. A negligible amount of the incident energy is coupled at 45°, causing a nearly 100% vignetting in the monocentric fiber coupled imager. This is the motivation for using a beam deflector, such as a micro-prism array, to redirect incident light and increase coupled energy.

4.3 Radial micro-prism array design and analysis

We require an analytical approach for calculating the geometry of radial micro-prism array, especially the prism facet angle as a function of position across the curved input face. This is in general a function of the objective lens numerical aperture. However, the coupling for the chief ray can be used as a straightforward design metric, accurate to within the cone-angle of the focusing light.

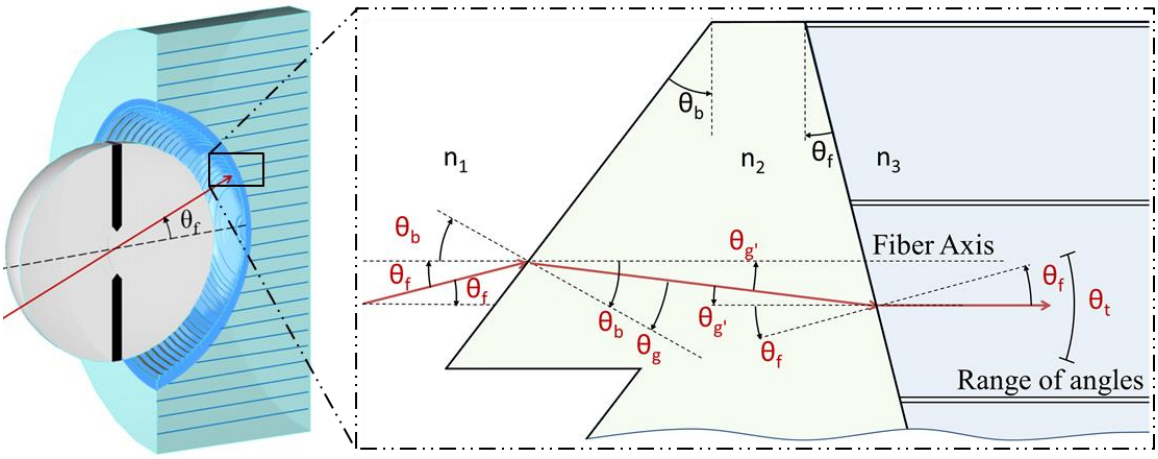

Figure 4-7: Illustration of the cross-section of the radial microprism array and fiber bundle in conjunction with the monocentric lens, and a ray optics schematic of propagation of light through micro-prism array and fiber.

4.3.1 **Analytical solution to micro-prism array**

Figure 7 illustrates a system where chief rays passing through the monocentric system are incident on the radial micro-prism array and refracted into the fiber bundle. The facet angles of the individual fibers are approximately equal to the chief ray angle with respect to the object scene in an ideal monocentric system. This means that the chief ray is always incident normal to the fiber surface, transmitting through without refraction and incident on the core/cladding wall at same angle as the field. Adding a higher index micro-prism material onto the curved image surface refracts the rays at angles above the normal of the fiber facet. Rays that would have been above the axial critical angle can be totally internally reflected, depending on the angle of refraction by the prism, and couple to the fiber. The interaction of light at the prism and fiber facet interfaces can be derived from surface refraction to be:

$$n_1 \sin(\theta_f + \theta_b) = n_2 \sin(\theta_g) \quad (1)$$

$$n_2 \sin(\theta_g - \theta_f) = n_3 \sin(\theta_f - \theta_t) \quad (2)$$

where in Eq. (1) n_1 is the refractive index of the medium between the ball lens and the prism, n_2 is the refractive index of the prism itself, θ_f is the field angle, θ_g is the angle of refraction with respect to the prism's normal, and θ_b is the blaze angle of the prism. Eq. (2) describes the refraction between the prism and the core where n_3 is the refractive index of the fiber core, $\theta_{g'}$ is the angle of refraction after the prism with respect to the optical axis, and the θ_t is the tolerance angle. Note that θ_f is used as both the field angle and the

angle of the facet since, as previously stated, the chief ray of each angle is equal to the corresponding facet angle. Solving for the angle of refraction after the prism with respect to the normal for Eq. (2) yields:

$$\theta_{g'} = \sin^{-1}\frac{n_3 \sin(\theta_f - \theta_t)}{n_2} - \theta_f \tag{3}$$

Using trigonometric identities and substituting the summation of $\theta_{g'}$ and θ_b for θ_g for Eq. (1) yields:

$$n_1 \sin(\theta_f + \theta_b) = n_2 \sin(\theta_{g'} + \theta_b) \tag{4}$$

$$n_1 \sin(\theta_f)\cos(\theta_b) + n_1 \cos(\theta_f)\sin(\theta_b) = n_2 \sin(\theta_{g'})\cos(\theta_b) + n_2 \cos(\theta_{g'})\sin(\theta_b) \tag{5}$$

$$n_1 \sin(\theta_f) + n_2 \sin(\theta_{g'}) = \tan\theta_b (n_2 \cos(\theta_{g'}) - n_1 \cos(\theta_f)) \tag{6}$$

Solving for the blaze angle for a range of field angles yields a variable micro-prism array facet angle as a function of field angle with the following equation:

$$\theta_b = \tan^{-1}\frac{n_1 \sin\theta_f + n_2 \cos\theta_{g'}}{n_2 \cos\theta_{g'} - n_1 \cos\theta_f} \tag{7}$$

The tolerance angle (θ_t) defines the angle of refraction inside the fiber core, and ultimately establishes the angle of divergence when exiting the fiber. For example, if the tolerance angle was set to be 0° the propagation of the chief ray would be on axis with the fiber and reduce the angle of divergence of the chief ray to 0°. This is ideal in terms of

output light coupling, but involves performance trade-offs that will be discussed in the next section.

4.3.2 **Moldable radial micro-prism array**

It is possible to define a radial microprism array that would be extremely difficult to fabricate, such as one with an unattainable index of refraction. In fact the simplest method of fabrication, and the one most compatible with volume manufacture, is a structure that can be molded or embossed. This creates two facets for the micro-prism array: an input facet, and a release facet. The input facet is the optically functional part of the prism which serves to refract the beam into the fiber core. The release facet is a mechanical constraint of the molding. Complex molding processes or materials may allow for sharply tilted microprisms, or even Fresnel lens like structures that involve total internal reflection [53]. For our design, we assumed that the release facets are arranged perpendicular to the optical axis of the system, allowing for the micro-prism mold master to be pressed into a prism material (e.g., a thermally or UV-curable epoxy) and then removed. However, both the input and release facets are optical surfaces that refract and transmit the focused beam. Rays incident on the input facet refract at angles below the normal of the fiber face to be totally internally reflected and transmitted in the corresponding fiber, while the release facet refract rays larger than the incident angle and result in a loss in coupling efficiency for the corresponding fiber. Unless the microprism pitch is small compared to the optical fiber core diameter, this is a significant factor in prism design. As Fig. 8 illustrates, for a micro-prism array molded in contact with the imaging surface, fibers illuminated only by light passing through the release facet will have low or no signal power. Figure 8(a) depicts

a scenario where the scene would vary in brightness periodically, creating an image with fibers that appear to be “on/off”. Alternatively, moving the prism surface further from the image surface and slowly varying blaze angle allows a larger region of the microprism array to be illuminated by a converging beam, dividing the energy between the input and release facets. This distributes power across all fibers because for any field angle two separate focused beams are generated: an enhanced coupling beam from the input facets, and a loss/noise beam from the release facet shown in Fig. 8(b). This loss/noise signal is incident on the fiber bundle at an even larger angle, and so most of the power does not couple to the guided mode. Instead, it propagates in the cladding and through the fibers.

4.3.3 **Micro-prism facet efficiency and micro-prism array design**

The divergence of the focused beam when exiting the fiber is dependent on tolerance angle described in Eq. (3). If the tolerance angle is selected to be 0°, the chief ray will refract and propagate directly down the fiber’s axis, minimizing the divergence when exiting the bundle. However, the maximum angle of refraction through the prisms is dependent on the finite index of the microprism material and a 90° maximum fabricable blaze angle. This means that at some point along the field of view the useful facet area of the radial micro-prism array will no longer be illuminated by any significant portion of the focused beam. On the other hand, the tolerance angle may be selected to be close to the axial critical angle of the fibers, so that the maximum amount of light will propagate inside the fiber. Although the coupling efficiency is maximized, the divergence angle of the rays when exiting the fiber is also at a maximum. The efficiency of the overall system is also determined by the tolerance angle of the prisms and the field of view. The field of view is

also considered in calculating the coupling efficiency since projection of the chief ray with respect to the prism facets determines the micro-prism efficiency. The increase in field of view reduces the projection of the input facets due to the increase in blaze angles of prism array. The size of the release facets increase as a consequence of the previous statement, but also due to the increasing field of view along the circular image plane. The efficiency equation is given by:

$$h = \frac{P_{in}}{P_{in} + P_{rel}} \tag{5}$$

where η is the efficiency, P_{in} is the projection of the input facet, and P_{rel} is the projection of the release facet, where both projections are towards the center of lens symmetry. The prism should ideally be made of extremely high index of refraction material to minimize the blaze angle required. This reduces the projection of the release facet while simultaneously increasing the projection of the input facet. However, we are limited to commercially available optical epoxies for the micro-prism array. Figure 9 describes the coupling efficiency of the system as a function of field angle and tolerance angle for a fiber core/cladding of 1.81 to 1.48, and a moldable prism with refractive index 1.56. This is the index of refraction of SU-8 photopolymer [54].

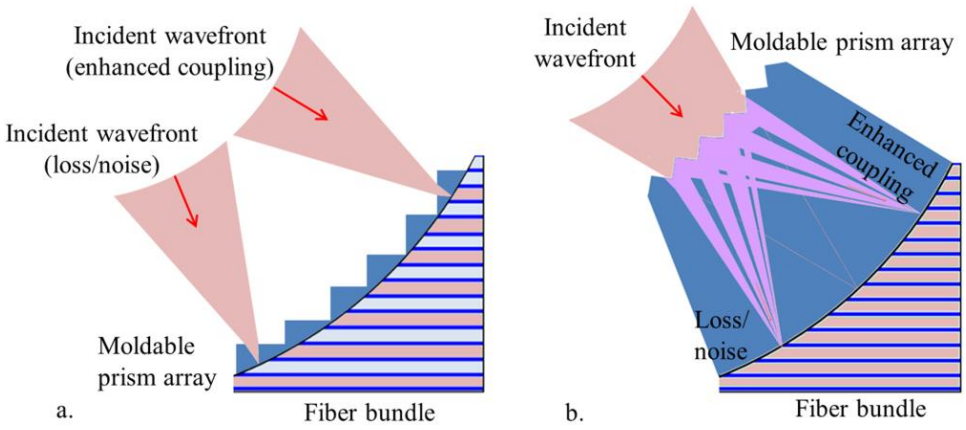

Figure 4-8: Illustration of a focused beam incident on a micro-prism array molded on the a) polished input surface of the fiber bundle, b) micro-prism array molded with a non-zero thickness onto the polished fiber bundle. Colored fibers signify coupling from the focusing beam.

If the micro-prism array is selected to guide the chief ray along the fiber optical axis for all angles ($\theta_t = 0°$), the coupling efficiency drops dramatically to zero passed 35°. Since we are attempting to maximize the coupling efficiency, the initialization of the radial micro-prism array does not begin until it reaches the 30° field angle. This means that the facet coupling efficiency is effectively unity until it reaches 30° field of view, as depicted by the black line in Fig. 9(a). As the field of view increases, the tolerance angle remains at 30° throughout the rest of the field of view maximizing the coupling efficiency of the prism for the given micro-prism index material. The blaze angle with respect to the optical axis of the system also increases as the field of view increases, thereby reducing the prism facet efficiency. However, the scene is made brighter with the prisms than without, resulting in an advantage over a polished-bare fiber bundle. The radial micro-prism array's blaze angle will vary as a function of field with a constant pitch of 25µm that follows along the radius of the fiber bundle. The choice of minimum prism pitch reflects the structural accuracy of features formed by low-cost embossing; too short a pitch would mean that the rounding of the prism edges covered a significant fraction of the surface area. The pitch of 25µm was

chosen as it was the shortest prism pitch available from commercially available micro-prism array sheets, which have been developed for use in liquid crystal display backlighting. For rays to be split across the micro-prism array and prevent dark bands from forming on the transferred image, the cone exiting the ball lens must intercept at least one full period for any field angle. Examining the geometrical spot size in Zemax for a field angle of 52°, we found that a prism substrate thickness of 390μm satisfies this constraint.

The final design of the chirped microprism array is shown in Fig. 10 with a constant pitch and using Eq. (3) and Eq. (7) from the previous section to determine the blaze angle as a function of the field of view. The microprism array can be diamond turned in a radial geometry on a master-mold using current manufacturing processes. The surface is smooth up to the field angle of 30˚, where the coupled light reaches the limits of the NA 1 fiber transmission. Above the angle, the microprism facets begin. At first, the input facet area is much larger than the release facet area, and the tilt angle is relatively small. As the field angle increases, the fraction of the area needed for prism molding increases, as does the tilt angle needed to keep the signal within the range needed for transmission.

4.3.4 **Optical response of radial micro-prisms**

Having used geometrical optics to design the microprism array, our next step is to model the optical response to determine the effect of the segmented aperture on the system impulse response, including diffraction effects. Figure 11 shows the cross section of a FRED simulation employing the optimized micro-prism structure with the glass F/# 4.4 singlet lens (BK7) with a 45° field angle, where we located 3x3 fiber arrays to observe the optical transfer from the two illuminated regions of the curved-face fiber bundle. A single

focused signal is split into two beams by facets of the radial micro-prism array. Rays refracted by the input facet are redirected and coupled into the fiber core, whereas rays refracted by the release facet are incident onto a separate 3x3 fiber array and refracted into the cladding. Figure 11(c) shows a polychromatic MTF calculation of the signal beam from the 45° incident light on the surface of the fiber bundle. A drop in resolution can be seen in the tangential plane due to astigmatism from the prism array and chromatic aberrations from the single glass lens and index of the micro-prism (1.56). Using an achromatic lens in conjunction with the micro-prism array can compensate for the chromatic aberrations. The fiber pitch is the limiting factor with a pitch of 8μm which corresponds to a maximum resolution of 62.5 cycles/mm. Light refracting into the cladding results in either loss of energy to the system, or noise in additional fibers. Figure 11(d) also shows a significant reduction in divergence of the beam emitted from the fiber, as compared to the beam emitted from an unmodified (spherically polished) fiber bundle for the same field angle. Integrating over the region of the sensor, we quantified an increase in brightness by a factor of 3.2 in comparison to the unmodified fiber bundle. Figure 12 shows that at this field angle, the polished input fiber couples a negligible portion of the focused beam, while the prism facets transfer approximately 50% of the incident energy into the useful coupled mode. The microprism facet apertures that split the focusing beam also cause diffraction, and there is some geometrical aberration caused

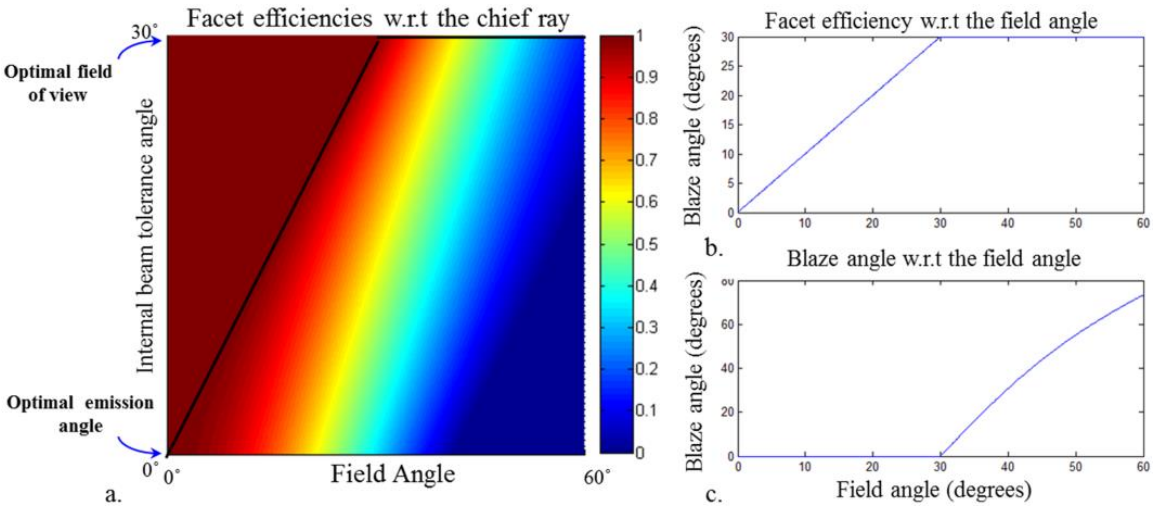

Figure 4-9: a) 2-dimensional facet efficiency color plot as a function of field angle and tolerance angle, b) chosen facet efficiency for micro-prism array, c) blaze angle of prism array with respect to the field angle.

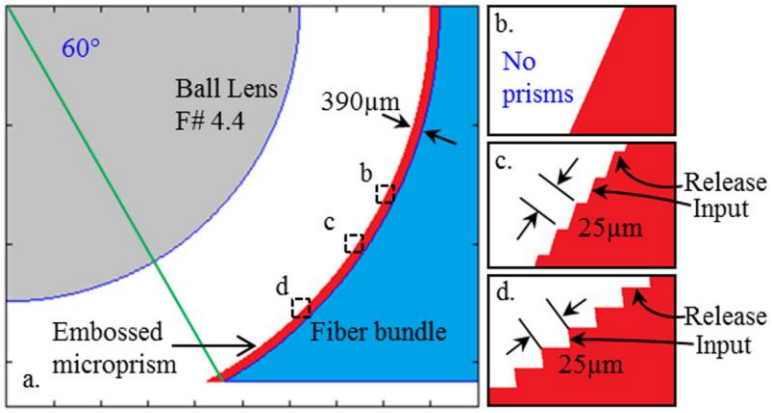

Figure 4-10: a) Schematic of ball lens system with an embossed micro-prism array on the input surface of the fiber bundle, b) region with no prisms, c, d) regions with micro-prism array. The microprism array has a thickness of 390µm.

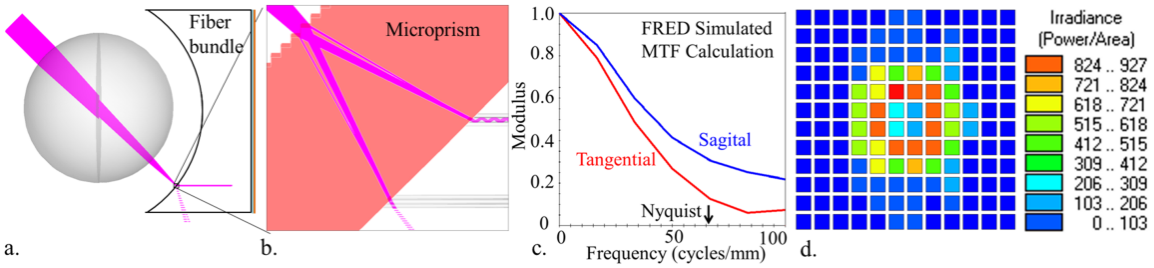

Figure 4-11: a,b) Cross section of a 3-D FRED simulation of the micro-prism array increasing coupling efficiency at a field angle (45°) larger than the axial critical angle, c) polychromatic MTF calculation of signal beam on surface of fiber bundle, d) irradiance plot on a pixel array.

by the prism itself. The diffraction impulse response shown in Fig. 12 confirms that the microprism sub-aperture, which is effectively rectangular in shape, reduces resolution in the direction perpendicular to the aperture restriction. These effects become more prominent with increasing field.

These calculations show that while microprisms can increase signal intensity at angles greater than 30˚ relative to a spherically polished fiber bundle, there is also significant loss from the projection of the useful microprism facet at the illuminating field angle. The incident light refracted by the release facet of the microprism is incident on the fiber bundle at even larger angles, previously shown in Fig. 8(b), and little of this energy can couple to the detector. However, with round fibers some of the energy couples via skew rays, even for very large angles of incidence. So to obtain an estimate of the resulting signal to noise, we quantified the ratio of coupling into the fibers and transmission to the detector between the input and release facets using a ray-based nonsequential FRED simulation. At each field angle, we calculated the energy efficiency through the microprism facet (signal), and also calculated the illumination and coupling (noise) that arrive at this region by refraction of a slightly smaller field angle through the release facet of a nearby region of the microprism array, and skew ray coupling through the fiber bundle. The

resulting signal to noise ratio at the detector is shown as a function of field angle in Fig. 13. For field angles less than 30˚, there is no prism structure, and therefore no source of noise; the high SNR in this region is indicated by a dashed line. Above 30˚, the SNR decreases overall as field angle increases. The local SNR depends on where the incident light illuminates the microprism: signal is high when the beam is centered on a useful microprism facet and low where the beam is centered on the release

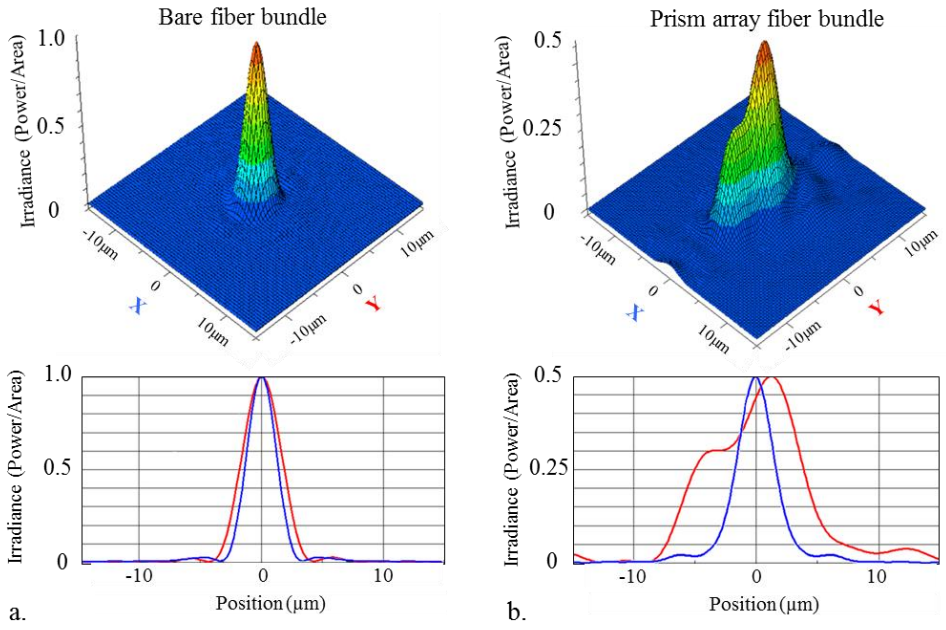

Figure 4-12: Irradiance spread function at 45° on surface of the a) polished input fiber bundle, b) input surface of the fiber bundle after being deflected by the prism array.

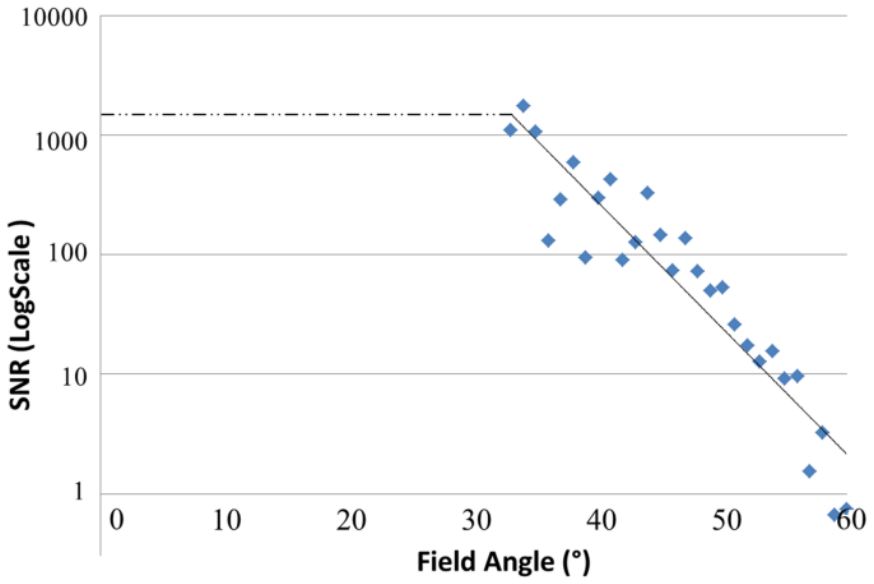

Figure 4-13: FRED calculation of signal-to-noise ratio of the input and release facet beams incident on groups of 3x3 fibers.

facet. So there is significant local variation in the calculated SNR values. Setting 100:1 (20dB) as a minimum SNR, we see the maximum useful field of view for microprisms embossed with a 25μm pitch and this 1.56 index of refraction would be between 90˚ and 100˚. This is a significant increase on the approximately 60˚ field of view possible using straight fiber bundles. Increasing the microprism index would further increase the useful field of view.

4.4 Proof of concept

To demonstrate microprism-enhancement of fiber coupling, we made a monocentric singlet lens and illuminated a straight N.A. 1 fiber bundle where the concave input surface covered over 100˚ field of view, nearly double the angular acceptance possible with a smooth spherical surface. The optimized design shown in Fig. 10 calls for a chirped spatial period prism structure, and the best way to test signal coupling is with a

high resolution focal plane index matched to the rear surface. For this first proof of principle, we fabricated microprism structures by embossing local regions of SU-8 photoresist with a constant spatial period linear prism array mold, and recorded the transmitted image by relay imaging the back surface of the fiber bundle onto digital SLR camera.

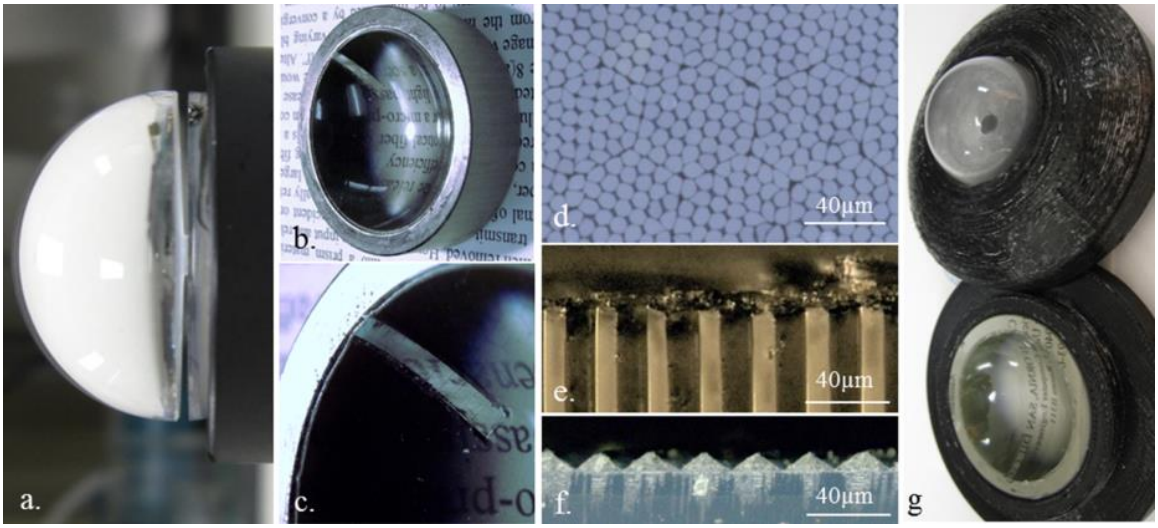

Figure 4-14: a) F/# 4.3 BK7 ball lens, b) curved-face fiber bundle with microprism array, c) close up of microprism array , d) microscope image of fiber, e) top view of molded micro-prism array structure, f) cross-section of Vikuiti BEF II 90/24 microprism array, g) ball lens and fiber bundle in 3D printed mount.

We constructed an F/4.3 monocentric singlet lens by cutting an aperture stop into a solid 24.24mm diameter BK7 sphere. The aperture was formed by cutting a deep slot into the perimeter of the lens with a diamond saw, rotating the lens until only a post approximately 2.80mm diameter remained at the center, then filling the kerf with black shims and UV-cured optical adhesive to block stray light and retain structural integrity. The result was a lens with a focal length of 17.8mm, and with a ZEMAX modeled 9.76µm RMS spot radius and 48 lp/mm at MTF50 for polychromatic light. The lens was tested using a NA 1 fiber bundle polished with a spherical input surface of radius 17.8mm and a

flat output surface. The fibers were arranged in an irregular hexagon closely-packed array with a 7 to 8 µm pitch, indicating a Nyquist-limited resolution of approximately 70 lp/mm. The singlet lens and fiber bundle were attached to two sides of a 3D printed mount, threaded to allow for focus, seen in Fig. 14.

We obtained a periodic linear prism array with a constant blaze angle of 45° and a pitch of 25µm from 3M (Vikuiti BEF II 90/24). Ideally, the microprism array should be made of annular rings and a variable blaze angle, but this structure is approximately correct for a small region of our design at a 45° field angle. A 2mm thick strip of the prism was molded onto a spherical polydimethylsiloxane (PDMS) handle with an approximate radius of 17.80mm. This negative PDMS mold was then used to make the positive spherical mold of optical adhesive (n = 1.56) onto the fiber bundle with the desired thickness of 0.390mm by offsetting the PDMS mold from the polished input surface of the fiber bundle. The molded prism was positioned on wide field of view regions from approximately 27 to 52°. PDMS was used as the molding material in order to prevent adhesion of the mold to the adhesive during lift off. The central aperture of the fiber bundle (the surface covering a field of view less than 27°) did not have a prism array, and instead had a spherical corrective surface to equalize the optical path length for all fields. Figure 14(f) shows the embossed microprism facets.

The imager was arranged 2 meters away from a wall covered with an assortment of resolution targets. In a similar setup to that used when measuring the divergence of the fiber bundles, we used a Canon DSLR camera with an F/2.8 lens to capture the image formed by the monocentric fiber coupled system. One limitation of this arrangement is that the light emitted from the fiber bundle can cover an angular extent far larger than the 10°

half field of view captured by the F/2.8 relay lens. The final fiber-coupled imager for this focal length will use a large format (full frame) CMOS image sensor, but the cost of this type of sensor did not allow their use for these proof-of-principal tests of microprism structure. Measuring the on-axis performance using Imatest software for the polished-bare fiber bundle produced a baseline resolution of 68cycles/mm at a modulus of 0.1 for our system, confirming that the fiber bundle rather than the lens was the resolution limit.

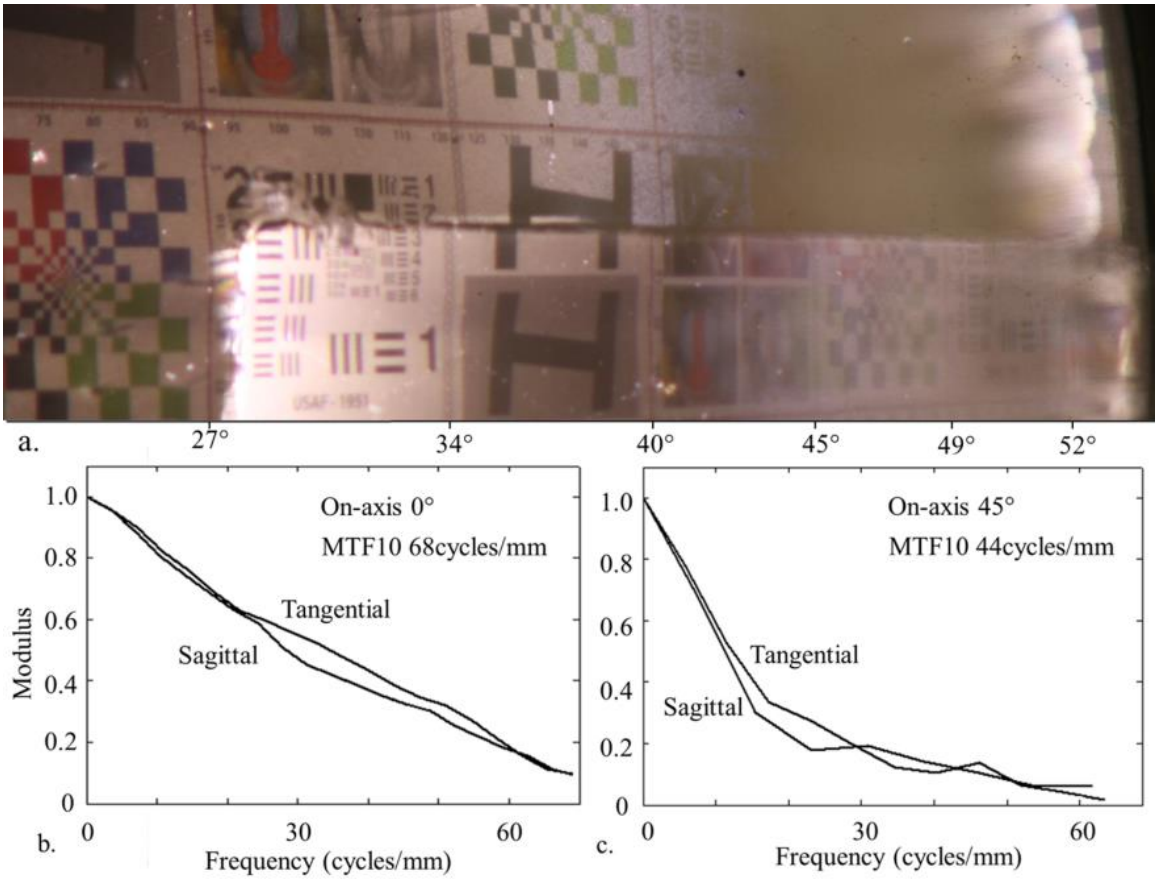

Figure 4-15: Photograph of image transferred through fiber bundle both with a smooth spherical surface (upper half) and with a molded prism (lower half) over the region from 27° to 52° field angle. The prism array extends the field of view where the polished bundle no longer transmits a significant signal. b,c) Slant edge chart MTF measurements at on-axis and 45° off axis.

Figure 15(a) shows the spherically corrected surface directly above the sectioned micro-prism array to have noisy background in the wider field of view areas. Since the fibers are closely packed and dense, rays that do not couple into the fibers are refracted and reflected in other core/cladding regions, effectively becoming stray light and background noise for other fields. These are the same areas where the coupling efficiency for the bare fiber bundle has dropped significantly, and background noise dominates most the image scene. Figure 15(b) shows a comparison of the resolution for the molded prism bundle revealing no significant changes on axis for the spherical corrective region. Shifting the camera to the region of the prism array captures light form both the spherically corrected and prism molded surface for comparison in resolution seen in Fig.15(c). A resolution of approximately 44 cycles/mm at a modulus of 0.1 was measured at the 45° field of view region for the calculated signal enhancement blaze angle. Aberrations associated with the prism array, in addition to any imperfections in the molding process, caused a decrease in resolution in contrast with the on-axis MTF. Overall, however, it is clear that the region of microprism array has increased the field of view while maintaining some resolution, and considerably decreased the noise that would have otherwise been present from the uncoupled rays.

The output of the fiber bundle has a transition from high-index fiber core to air, which prevents some large-angle rays coupled into the fiber from exiting. To provide a more representative sample of the transferred image we molded an 80° holographic diffuser using PDMS on the output surface of the fiber bundle. This causes the light incident on the rear surface of the fibers to scatter into a wide angle, reducing signal power at any given field position, but allowing a single image to capture the full field. The diffusive surface

was on the order of tens of microns, reducing the resolution of our image, but provided an observation of enhanced signal coupling from the prism array. Figure 16 shows a panoramic image of individually stitched images taken by shifting the relay camera across the fiber bundle. Close examination of the prism array regions reveals the brightness significantly enhanced, and noise reduced, in the wide field of view in comparison to the spherically corrected region above. We measured the intensity at the 45° field of view of a white background image to be brighter by approximately a factor of 3 in comparison to the polished region, confirming our results in simulation from the previous section.

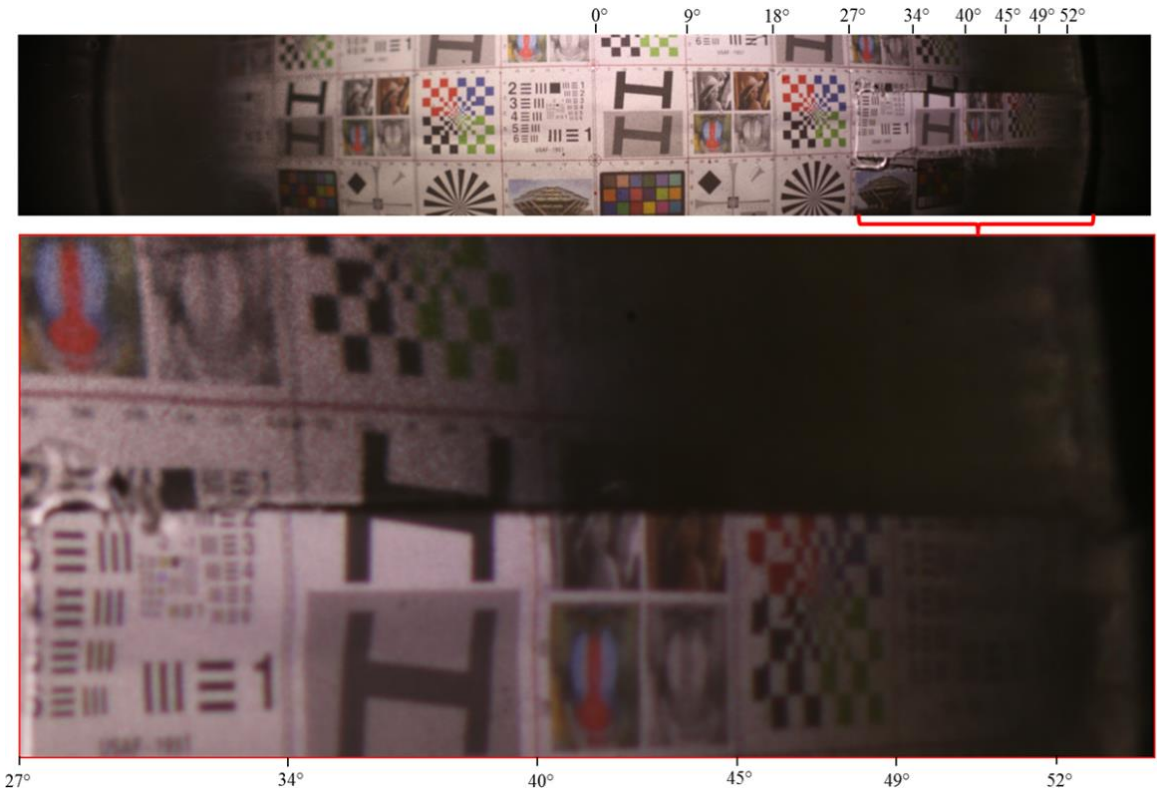

Figure 4-16: Stitched image of prism array molded bundle with a diffusive output surface. The image was stitched from several images at a constant 1 sec exposure and ISO 400.

4.5 Conclusion

We have shown that the field of view possible for images coupled from a spherical field of view via straight fiber bundles can be significantly enhanced using a beam-deflecting structure close to the spherical image surface. Monocentric fiber coupled imagers benefit from a radially symmetric system that do not suffer from coma or astigmatism, and can be utilize a curved image surface. This beam-deflection can be accomplished by multiple types of structures, both refractive and diffractive. We described analysis and an experimental proof-of-principle investigation of the use of microprisms directly embossed onto the spherical fiber bundle. The optimum embodiment of this general concept may involve diffractive, rather than refractive beam deflections. One method is to create a chirped volume hologram located near to the image surface. Another direction is the use of surface plasmon antennas directly on the image surface, in contact with the high index fibers [55]. These techniques offer for the volume manufacture of fiber-coupled wide-field imagers, which may ultimately support the wafer-scale fabrication of fiber-coupled image sensors for low-cost wide-angle imaging.

5. Thesis Conclusions and future directions

I have demonstrated that curved-input fiber bundles in an optical system are effective curved focal surfaces that can substitute for a flat focal plane. The eye model's presented in Chapter 2 is an example of a novel curved-focal fiber coupling optic that can be used as a test-bed for characterizing vision-based optical devices, including display systems (i.e. head mounted displays). The wearable telescopic contact lens presented in Chapter 3 demonstrated a new low vision aid in the form of a compact folded-optic scleral lens with the potential to aid patients suffering from AMD. Chapter 4 revealed the inherent limitations of using a single curved-face bundle in wide-field imaging cameras, and a potential solution for increasing the field of view at the wafer scale by molding a radial micro-prism beam deflector on the input surface of the fiber bundle.

In an effort to commercialize fiber coupled imaging in conjunction with CMOS sensors, further research is required in manufacturing and bonding the CMOS sensor to a fiber bundle at the wafer-level. Certain artifacts such as Moiré pattern have been observed when two periodic surfaces (fiber bundle and CMOS imaging sensor) are bonded ton another [57]. Calibrations will be required in order to compensate for these artifacts. Tapered fibers are also an alternative solution that can increase the field of view without

sacrificing light collection [48,49]; however, the embossed radial micro-prism array I presented in Chapter 4 is a more cost-effective and manufacturable method. The technology transition of curved focal surfaces requires further research in implementing fiber bundles in mass manufacturing. Developing a process to integrate fiber bundles at the wafer level can bridge the gap between a flat focal plane to an effectively curved CMOS sensor.

Research is currently underway for developing and fabricating curved CMOS image sensors, though no commercially available product has reached the market to this date. The need for a curved image surfaces is growing as imaging-based consumer products, such as cell phone cameras, become even more common, compact, and higher in resolution. Sony recently developed and publicized a cylindrical CMOS sensor with plans for integration in an upcoming consumer product [56], although details of the resolution, curvature, or cost have not yet been made public. Until high resolution and curved CMOS sensors in a wide range of geometries become commercially available, fiber bundles have the potential to be an adequate substitute for implementing a curved focal surface into an optical system.

References

1. Warren Smith, *Modern Optical Engineering.* SPIE Press, 4th Edition 2007.

2. M. Szinte, P. Cavanagh, "Apparent motion from outside the visual field, retinotopic, cortices may register extra retinal positions," PLOS ONE, Vol: 7(10) (2012).

3. W.R. Hendee, P.N.T Wells, *The Perception of Visual Information*. Springer, 2nd ed. 1997

4. S. Rim, P. Catrysse, R. Dinyari, K. Huang, and P. Peumans, "The optical advantages of curved focal plane arrays," Opt. Express 16, 4965-4971 (2008).

5. T. Sutton, "Panoramic photography," Photon. J. 6, 184–188 (March 1860)

6. D. J. Brady, M. E. Gehm, R. A. Stack, D. L. Marks, D. S. Kittle, D. R. Golish, E. M. Vera, S. D. Feller, "Multiscale gigapixel photography," Nature 486, pg. 386-389 (2012)

7. B. A. Flusberg, E. D. Cocker, W. Piyawattanmetha, J. C. Jung, E. L. M. Cheung, M. J. Schnnitzer, "Fiber-optic fluorescence imaging," Nature Methods, Vol 2, 941 -950 (2005)

8. Jorge L. Alió, Joshua Ben-nun, José L. Rodríguez-Prats, Ana B. Plaza. Visual and accommodative outcomes 1 year after implantation of an accommodating intraocular lens based on a new concept. Journal of Cataract and Refractive Surgery 2009, 35(10):1671-1678

9. S.P. Kelly, and A Jalil. Wrong intraocular lens implant; learning from reported patient safety incidents. Eye (Lond) 2009, 25(6):730-734

10. Patricia A. Piers, Silvestre Manzanera, Pedro M. Prieto, Nicolas Gorceix, Pablo Artal. Use of adaptive optics to determine the optimal ocular spherical aberration. Journal of Cataract and Refractive Surgery 2007; 33(10):1721-1726

11. P. Artal, S. Manzanera, P. Piers, and H. Weeber. Visual effect of the combined correction of spherical and longitudinal chromatic aberrations. Opt. Express 2010; 18:1637-1648

12. Pier Giorgio Gobbi, Francesco Fasce, Stefano Bozza, Rosario Brancato. Optomechanical eye model with imaging capabilities for objective evaluation of intraocular lenses. Journal of Cataract Refractive Surgery 2006; 32(4):643-651

13. Pier Giorgio Gobbi, Francesco Carones and Rosario Brancato. Optical eye model for photorefractive surgery evaluation. Proc. SPIE 1999; 3591:10-21

14. Agnieszka Barcik, Jerzy Nowak, Damian Siedlecki, Marek Zając and Józef Zarówny. Physical model of human eye with implantable intraocular lenses. Proc. SPIE 2008; 7141(71411A):1-8

15. P. Piers, N. Sverker Norrby, and U. Mester, Eye models for the prediction of contrast vision in patients with new intraocular lens designs. Opt. Letters 2004; 29:733-735

16. Thom Terwee, Henk Weeber, Marrie van der Mooren, Patricia Piers. Wavefront measurements of diffractive and refractive multifocal intraocular lenses in an artificial eye. J Refract Surg. 2008; 24(3):308-11.

17. S. Norrby, P. Piers, C. Campbell, and M. van der Mooren, "Model eyes for evaluation of intraocular lenses", Appl. Opt. 46, 6595-6605 (2007)

18. C.E. Campbell "Wavefront Measurement of Diffractive and Refractive Multifocal Intraocular Lenses in an Artificial Eye", Journal of Refractive Surgery, 24(3) 308-311, (2008).

19. Ravi C Bakaraju, Klaus Ehrmann, Darrin Falk, Arthur Ho, and Eric Papas. Physical human model eye and methods of its use to analyze optical performance of soft contact lenses. Opt. Express 2010; 18(16):16868-16882

20. H. Liou and N. Brennan. Anatomically accurate, finite model eye for optical modeling. J. Opt. Soc. Am. A 1997; 14:1684-1695

21. R. Navarro, J. Santamaría, and J. Bescós. Accommodation-dependent model of the human eye with aspherics. J. Opt. Soc. Am. A 1985; 2: 1273-128.

22. D. Atchison and G. Smith, Optics of the Human Eye (Butterworth-Heinemann, 2000).

23. Hancock, Jed J. The design, fabrication, and calibration of a fiber filter spectrometer. PhD Thesis. University of Arizona, Tucson, 2012.

24. Stefan Pieh, MD; Patrick Marvan, MD; Birgit Lackner, MD; Georg Hanselmayer, MD; Gerald Schmidinger, MD; Rainer Leitgeb, PhD; Markus Sticker, PhD; Christoph K. Hitzenberger, PhD; Adolf F. Fercher, PhD; Christian Skorpik, MD. Quantitative Performance of Bifocal and Multifocal Intraocular Lenses in a Model Eye: Point Spread Function in Multifocal Intraocular Lenses. Arch Ophthalmol.2002;120(1):23-28

25. http://www.imatest.com/products/test-charts/sfr-plus-test-charts/

26. D. S. Friedman, B. J. O'Colmain, and I. Mestril, "2012 Fifth Edition of Vision Problems in the U.S.," http://www.visionproblemsus.org/introduction/acknowledgments.html.

27. C. Dickinson, Low Vision: Principles and Practice (Buttorworth-Heinemann, 1998).

28. http://www.eschenbach.com/consumers-low-vision-devices-for-the-visually-impaired.htm

29. J. P. Szlyk, W. Seiple, D. J. Laderman, R. Kelsch, J. Stelmack, and T. McMahon, "Measuring the Effectiveness of Bioptic Telescopes for Persons with Central Vision Loss," J. Rehabil. Res. Dev. 37(1), 101–108 (2000).

30. S. S. Lane and B. D. Kuppermann, "The implantable miniature telescope for macular degeneration," Curr. Opin. Ophthalmol. 17(1), 94–98 (2006).

31. A. Isen, "Feinbloom miniscope contact lens," Encyclopedia of contact lens practice. 13, 53–55 (1963).

32. E. Tremblay, R. Stack, R. Morrison, and J. Ford, "Ultrathin cameras using annular folded optics," Appl. Opt. 46, 463-471 (2007).

33. E. J. Tremblay, I. Stamenov, R. Beer, A. Arianpour, and J. Ford, "Switchable telescopic contact lens," Opt. Express 21, 15980-15986 (2013).

34. http://www.acuvue.com/sites/default/files/content/us/pdf/M-09-14-00%201DAVM%20PI-FIG%20(website).pdf

35. http://www.acculens.com/Acculens%20Webinar%20March.pdf

36. http://www.sclerallens.org/about

37. http://www.reviewofoptometry.com/continuing_education/tabviewtest/lessonid/108308/

38. W. Benjamin, Q. Cappelli, "Oxygen Permeability (Dk) of Thirty-Seven Rigid Contact Lens Materials" Optometry & Vision, 79(2), pp. 103 – 111 2002

39. http://www.bausch.com/ecp/our-products/contact-lenses/aphakia/silsoft-and-silsoft-super-plus#.VPJoi_nF_0c

40. Imamura, Y., et al. "Use of perfluorocarbon liquid during vitrectomy for severe proliferative diabetic retinopathy." British journal of ophthalmology 87.5 (2003): 563-566

41. A. Arianpour, E. J. Tremblay, I. Stamenov, J. E. Ford, D. J. Schanzlin, and Y. Lo, "An Optomechanical Model Eye for Ophthalmological Refractive Studies," J. Refract. Surg. 29(2), 126-132.

42. H. Gross, F. Blechninger, B. Achtner, Handbook of Optical Systems, Survey of Optical Instruments. Wiley, 2008.

43. W.Y. Lau, C.K. Leow, A.K.C. Li, "History of endoscope and laparoscopic Surgery," World of Surgery, Vol. 21, Issue 4, 444-53 (1997).

44. J. A. Waidelich, Jr., "Spherical lens imaging device," U.S. patent 3,166,623 (19. January 1965).

45. R. Kingslake, A History of the Photographic Lens (Academic, 1989), pp. 49-67.

46. T. S. Axelrod, N. J. Colella, and A. G. Ledebuhr, "The wide-field-of-view camera," in Energy and Technology Review, (Lawrence Livermore National Laboratory, 1988).

47. J. F. Kordas, I. T. Lewis, B. A. Wilson, D. P. Nielsen, H.S. Park, R. E. Priest, R. Hills, M. J. Shannon, A. G. Ledebuhr, L. D. Pleasance, "Star tracker stellar compass for the Clementine mission". Proc. SPIE 2466, Space Guidance, Control, and Tracking II, 70 (1995).

48. J. Ford, I. Stamenov, S. Olivas, G. Schuster, N. Motamedi, I. Agurok, R. Stack, A. Johnson, and R. Morrison, "Fiber-coupled Monocentric Lens Imaging," in Imaging and Applied Optics, OSA Technical Digest (2013).

49. I. Stamenov, A. Arianpour, S. Olivas, I. Agurok, A. Johnson, R. Stack, R. Morrison, and J. Ford, "Panoramic monocentric imaging using fiber-coupled focal planes," Opt. Express 22, 31708-31721 (2014).

50. J. Shields, M. Karr, R. Johnson, and A. Burden, "Day/night whole sky imagers for 24-h cloud and sky assessment: history and overview," Appl. Opt. 52, 1605-1616 (2013).

51. J. J. Hancock, The Design, Fabrication, and Calibration of a Fiber Fil¬ter Spectrometer. Doctoral dissertation. University of Arizona, Tucson, 2012.

52. Cozannet and M. Treheux, "Skew rays in optical fibers," Appl. Opt. 14, 1345-1350 (1975).

53. L. Jing, H. Liu, H. Zhao, Z. Lu, H. Wu, H. Wang, J. Xu, “Design of Novel Compound Fresnel Lens for High-Performance Photovoltaic Concentrator,” International Journal of Photoenergy, Vol. 2012, 7 pages, 2012.

54. C. Reardon, A. Di Falco, K. Welna, and T. Krauss, "Integrated polymer microprisms for free space optical beam deflecting," Opt. Express 17, 3424-3428 (2009).

55. A. Smolyaninov, L. Pang, L. Freeman, M. Abashin, and Y. Fainman, "Broadband metacoaxial nanoantenna for metasurface and sensing applications," Opt. Express 22, 22786-22793 (2014).

56. K. Itonaga, US Patent 8,878,116

57. S. Olivas, A. Arianpour, I. Stamenov, R. Morrison, R. Stack, A. Johnson, I. Agurok, and J. Ford, "Image processing for cameras with fiber bundle image relay," Appl. Opt. 54, 1124-1137 (2015)